



SMaRT-OnlineWDN deliverable 4.3&4: Adaptation of transport equations and CFD Simulation of the transport phenomena and comparison with measured data

Denis Gilbert, Olivier Piller, Hervé Ung, Thomas Bernard, Mathias Braun, Andreas Korth, Reik Nitsche, Fereshte Sedehizade

► To cite this version:

Denis Gilbert, Olivier Piller, Hervé Ung, Thomas Bernard, Mathias Braun, et al.. SMaRT-OnlineWDN deliverable 4.3&4: Adaptation of transport equations and CFD Simulation of the transport phenomena and comparison with measured data. [Research Report] Irstea. 2015, pp.46. hal-03317871

HAL Id: hal-03317871

<https://hal.inrae.fr/hal-03317871>

Submitted on 8 Aug 2021

HAL is a multi-disciplinary open access archive for the deposit and dissemination of scientific research documents, whether they are published or not. The documents may come from teaching and research institutions in France or abroad, or from public or private research centers.

L'archive ouverte pluridisciplinaire **HAL**, est destinée au dépôt et à la diffusion de documents scientifiques de niveau recherche, publiés ou non, émanant des établissements d'enseignement et de recherche français ou étrangers, des laboratoires publics ou privés.



SPONSORED BY THE



Federal Ministry
of Education
and Research



Deliverables 4.3 & 4.4

Adaptation of transport equations

CFD Simulation
of the transport phenomena and
comparison with measured data

Dissemination level: Restricted

WP4

Transport Modelling

3 April 2015

SMaRT-Online^{WDN}

Online Security Management and Reliability Toolkit
for Water Distribution Networks

ANR reference project: ANR-11-SECU-006

BMBF reference project: 13N12180

Contact persons

Fereshte SEDEHIZADE
Olivier PILLER

Fereshte.Sedehizade@bwbt.de
Olivier.Piller@irstea.fr

CFD simulation of the transport phenomena and comparison with measured data

3 April 2015

Page 1

WP 4 – Transport Modelling

D4.3 Adaptation of transport equations

D4.4 CFD Simulation of the transport phenomena and comparison with measured data

List of Deliverables 4.3-4.4 contributors:

From Irstea

Denis Gilbert (denis.gilbert@irstea.fr) [WP4 leader]

Olivier Piller (olivier.piller@irstea.fr)

Hervé Ung (herve.ung@irstea.fr)

From IOSB

Thomas Bernard (thomas.bernard@iosb.fraunhofer.de)

Mathias Braun (mathias.braun@iosb.fraunhofer.de)

From TZW

Andreas Korth (andreas.korth@tzw.de)

Reik Nitsche (reik.nitsche@tzw.de)

From BWB

Fereshte SEDEHIZADE (fereshte.sedehizade@bwb.de)

Work number	package	4.3-4.4	Start date:		01/04/2012
Contributors id		Irstea	IOSB	TZW	BWB
Person-months participant		10	5	8	2
Keywords					
Imperfect Mixing – Dispersion – Transport modelling – CFD – Laminar – Turbulent – Design of Experiment					
Objectives					
Adapt the 1D model of transport by using 3D CFD and experiments, compare results of CFD and experiments					

Executive Summary

The main objective of the SMaRT-Online^{WDN} project is the development of an online security management toolkit for water distribution networks that is based on sensor measurements of water quality as well as water quantity. Pseudo-real time modelling of water quantity and water quality variables is the cornerstone of the project. Existing transport model tools are not adapted for online modelling and ignore some important phenomena that may be dominant when looking at the network in greater detail with an observation time of several minutes.

The aim of this deliverable is to report investigations by the SMaRT-Online^{WDN} partners about processes of contaminant mixing at T-junctions and transport in pipes.

Firstly, a bibliographical review of the problem of imperfect mixing is presented. For transport in a water distribution network, only cross-junction and double T junction should be considered. The double T is composed of two entries, one intermediate pipe and two outputs. The first entry is the straight one and the second is perpendicular to it, the same goes for the outputs. There are four parameters modifying the mass balance in a double T intersection mixing law: The Reynolds number at the middle of the intermediate pipe, percentage of flow at inlets, percentage of flow at outlets, distance between the two Ts. The present study is designed to raise previous limitations mainly for laminar regimes and high Reynolds numbers. For implementation of a 1D law for imperfect mixing, we build a lookup table based on CFD simulations and Kriging interpolation is used for entries that are not in the table.

Then, it was necessary to develop an in-house Kriging interpolation method. It is based on the original method, which is a two-step process, but optimisations of parameter and regression adjustments were necessary to adapt it for this particular study.

Next, design of experiments based on Delaunay triangulation method is detailed. The discretisation to calculate the entire domain is too large to be fully investigated. The Delaunay triangulation method chooses the next points to simulate that minimise the error between interpolated law and simulation or experiment.

Following from this, the mesh convergence is tested for validation of the mesh size. It was found that a mesh of 1 million cells is sufficient for almost all simulations.

Then, more than 250 simulations have been made with introduction of a contamination at the second inlet. When the first inlet flow is dominated, the mixing is perfect. The mixing becomes imperfect when the inlet flow at first entry increases. That behaviour shift is more pronounced for the laminar case whatever the inter T distance and progressive in the turbulent case. The mixing tends towards perfect mixing when the inter T distance increases, it is almost perfect for $L = 20D$ in the turbulent case. It also decreases when the Reynolds number increased but tends to an equilibrium that may not be the perfect mixing.

Next, results of interpolation are compared with experiments. The experiments show a perfect mixing in the case where entry inlet 1 is dominated, which confirms the CFD simulation finding. Some discrepancies between simulations and experimentations can be observed for the laminar regime, which might be due to the difficulty in measuring very low flows in pipes, as well as gravity effects on the contaminant and conductivity sensors being at the centre of the tubes. A good matching can be seen in the cases $Re = 2,000$ and $Re = 5,000$.

To accelerate the convergence with CFD simulation that requires fewer cells, it was decided to combine two single T simulations to solve the double T problem. It has been found by

CFD simulation of the transport phenomena and comparison with measured data

comparison between full double T simulations and combined single T simulations that this method is working in laminar cases for most scenarios but not the turbulent case.

The complex geometry of the double T junction, when taking into account the joints, doesn't seem to affect the results much. It can't explain the differences with the experiments.

CFD simulation results were used to fill a lookup table with a non-dimensional indicator of the deviation from the perfect mixing. The mean concentration at outlet 1 is calculated; then the ratio from what is introduced is calculated; finally the perfect mixing contribution is subtracted. A system of equations was derived that generalises the case introduction of a contaminant only at inlet 2 to both of the inlets.

Finally, a software solution of the new transport model is proposed to be interfaced with any other hydraulic module.

Figures and tables

FIGURE 1: CROSS CONFIGURATION (FROM [1]) WITH 2 INLETS AND 2 OUTLETS.	8
FIGURE 2: DOUBLE T CONFIGURATION WITH 2 INLETS AND 2 OUTLETS.	9
FIGURE 3: THE 4 PRINCIPAL CONFIGURATIONS OF T-JUNCTIONS AND THEIR REPARTITIONS IN STRASBOURG WDN.	10
FIGURE 4: FREQUENCY OF REYNOLDS NUMBER FOR 3X100 T-JUNCTION OF STRASBOURG NETWORK.....	10
FIGURE 5: CONTOUR PLOT OF THE LOG-LIKELIHOOD FUNCTION WITH RESPECT TO THE SHAPE PARAMETER THETA AND THE REGULARISATION PARAMETER.	15
FIGURE 6: LEFT) DELAUNAY TRIANGLE; CENTER) INTERPOLATION FULL; RIGHT) INTERPOLATION WITHOUT POINT (1,0)	19
FIGURE 7: EXAMPLE OF SIMULATION RESULT CURVE OF MASS FLUX (LEFT: OUT1, RIGHT: OUT2).	21
FIGURE 8: RESULT FOR DISTANCE = 5D AND REYNOLDS = 1,000.....	21
FIGURE 9: RESULTS FOR REYNOLDS = 5000, LEFT) 5D, MIDDLE) 8D, RIGHT) 10D.	21
FIGURE 10: EXAMPLE OF FOR THE DISTANCE = 5D, REYNOLDS = 1,000: UP) BEFORE, DOWN) AFTER FIVE SIMULATIONS CHOSEN BY THE TRIANGULATION OF DELAUNAY.	22
FIGURE 11: COMPARISON OF RESULTS BETWEEN MESHES OF 1 000 000 AND 8 000 000 CELLS FOR CASE $Re = 1\,000$, $L = 5D$, $\%In1 = 70$; $\%Out1 = 50$. TOP) SCALAR; MIDDLE) VELOCITY MAGNITUDE; BOTTOM) YPLUS.....	25
FIGURE 12: POINTS OF SIMULATIONS, BLUE) CODE SATURNE ; ORANGE) CODE SATURNE (TWO T COMBINED, SEE PART 7) ; GREEN) FLUENT.	26
FIGURE 13: INTERPOLATION 4D KRIGING IN SPACE $\%In1$ (CALLED E1)/ $\%Out1$ (CALLED S1).	27
FIGURE 14: INTERPOLATION 4D KRIGING IN SPACE L/Re , CASE $\%In1$ AND $\%Out1 = 20/30/50/70/80$	28
FIGURE 15: REPRESENTATION OF SCALAR ON LONGITUDINAL SECTION OF DOUBLE T IN CASES $Re = 1,000$ FIXED, $L = 5D$ FIXED, AND $\%In1$ AND $\%Out1 = 30/50/70$	29
FIGURE 16 : PHOTO OF THE PILOT IN DRESDEN.	31
FIGURE 17: SCHEMA OF THE PILOT IN DRESDEN WITH A CONTAMINATION EXAMPLE.	31
FIGURE 18: COMPARISON BETWEEN CFD AND EXPERIMENTS: $Re = 1,000$ (BLUE CFD SIMULATIONS, RED EXPERIMENTS)	32
FIGURE 19: COMPARISON BETWEEN CFD AND EXPERIMENTS $Re = 2000$ (BLUE CFD SIMULATIONS, RED EXPERIMENTS).....	33
FIGURE 20: COMPARISON BETWEEN CFD AND EXPERIMENTS: $Re = 5,000$ (BLUE CFD SIMULATIONS, RED EXPERIMENTS).	34
FIGURE 21: CROSS-SECTION IN CASES 10D, $Re=1,000$, 80/20 AND 80/80	36
FIGURE 22: COMPARISON COMBINED, 5D $Re=1,000$	37
FIGURE 23: COMPARISON COMBINED, 10D $Re=1,000$	37
FIGURE 24: COMPARISON COMBINED, 5D $Re=2,000$	37
FIGURE 25: COMPARISON COMBINED, 5D $Re=5,000$	38
FIGURE 26: REAL GEOMETRY.....	39
FIGURE 27: COMPLEX MESH.....	39
FIGURE 28: COMPARISONS OF COMPLEX GEOMETRY, NORMAL GEOMETRY AND EXPERIMENTATIONS.	40
FIGURE 29: CHOICES FOR TRANSPORT CALCULATION, CROSS AND DOUBLE T.	43

TABLE 1: PARAMETER DOMAIN	18
TABLE 2: EXAMPLE DELAUNAY METHOD WITH ASSOCIATED ERRORS.	19
TABLE 3: RESULTS FOR SIMULATION CFD (NON EXHAUSTIVE)	20
TABLE 4: DELAUNAY POINTS FOR DISTANCE = 5D AND Re = 1.000.....	23
TABLE 5: MESH CONVERGENCE TESTS.....	24

Notation

XX/YY = (%In1 = XX and %Out1 = YY)

DNS: Direct numerical simulation

LES: Large eddy simulations

MCIA: Mésocentre de Calcul Intensif Aquitain

CINES : Centre Informatique National de l'Enseignement Supérieur

TZW: Technologiezentrum Wasser

Table of contents

Figures and tables	5
1. Introduction	8
2. Kriging Interpolation.....	12
Step 1- Regression model and maximum-likelihood parameter estimation	12
Step 2- Kriging Interpolation	15
3. Design of experiments and Delaunay Triangulation	18
4. The mesh convergence test	24
5. CFD Results.....	26
6. Comparison with the experiments	31
7. Acceleration by combining two single T-junctions.....	36
8. Complex Mesh.....	39
9. Toward a formulation 1D of the imperfect mixing	41
10. Implementation	43
11. Conclusion.....	44
12. Acknowledgements.....	45

1. Introduction

Mixing at cross and double T-junctions are being studied in this section. The network of TZW in Dresden permits the development and validation of the codes. Finally, the software and the method solutions will be demonstrated with application on three different real case studies.

In recent studies, Ho and Khalsa [1], Choi *et al.* [2], showed that mixing at junction is important regarding security and its assessment by calculation of the hydraulic quality state of the network. [1] developed and adjusted with experiments, the Bulk-Advective Mixing model BAM for cross-junction imperfect mixing depending on the Reynolds number at the inlets and outlets.

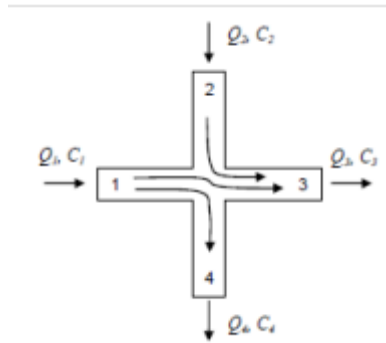


Figure 1: Cross configuration (from [1]) with 2 inlets and 2 outlets.

In the cross-junction configuration of Figure 1, there is a principal flow 1 where the inlet goes into the two-outlet direction 3 and 4 and the secondary flow where the inlet 2 is only going to the nearest outlet 3. For this configuration and within steady state condition, the pure BAM model reads:

$$C4 = C1$$

$$C3 = \frac{Q2C2 + (Q1 - Q4)C1}{Q3} \quad (1)$$

From Figure 1, it can be seen that $Q4 < Q1$ therefore $Q1 - Q4$ is positive. The complete BAM model [1] consists of combining the perfect mixing and the pure BAM model with the following equation:

$$C_{scaled} = C_{bulk} + s(C_{perfect} - C_{bulk}) \quad (2)$$

Where s is a coefficient that depends on the real state of the cross-junction; and C_{bulk} is calculated with **Eq. (1)**. They proposed to calibrate the s coefficient from experiments. Their results for X and N-junctions (or double T-junctions) is implemented in the Epanet-BAM module [3].

The AZRED model [2] proposes the use of a lookup table with interpolation or extrapolation for entries not in the table. It was validated on experimental values with a large range of flows. One

CFD simulation of the transport phenomena and comparison with measured data

limitation is the need for extrapolation for Reynolds ratios approaching zero or infinity. What is proposed in the SMART-Online^{WDN} project is to complete the two previous models to be applicable for a one-dimensional model such as Porteau and sir3S software solutions by the partners Irstea and 3S Consult [4; 5]. The approach is to develop a method with comparison and validation with the CFD model and laboratory experiments. Some results were published in [6; 7].

For the case of incomplete mixing of a double T junction or N junction, one configuration (**Figure 2**) is particularly interesting: this is when there are two inputs followed by an intermediate section then two outputs. In all other cases the mixing is either complete or close to being complete. The different velocities, diameters and length of the intermediate pipe will influence the mixing. The configuration has been chosen with equal diameters for all inputs and outputs. A statistical study showed that this represents most cases in the network. The whole phenomenon is driven by four variables: the average Reynolds number inside the connecting pipe, the Reynolds inlet fraction of one of the entries, the Reynolds outlet fraction of one of the outputs and the distance between the T junctions. For configurations with unequal pipe diameters, the flow rate should be used in place of the different Reynolds.

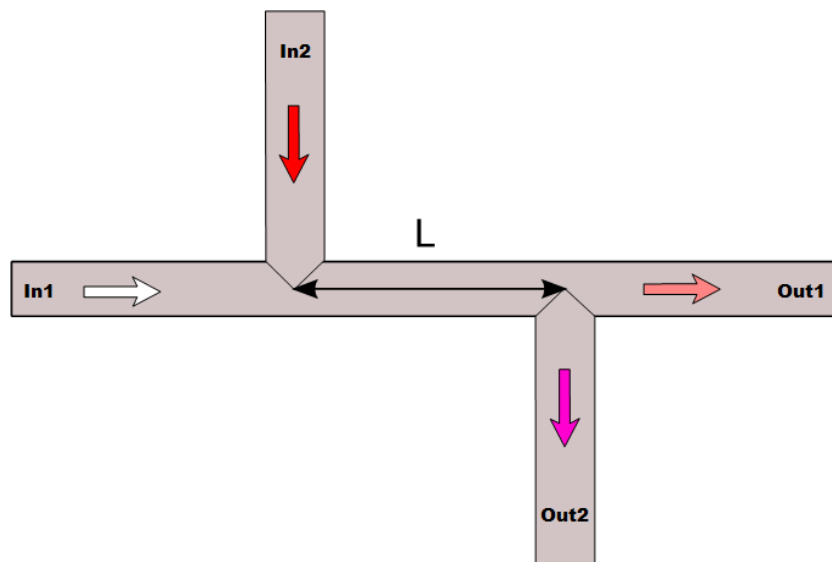


Figure 2: Double T configuration with 2 inlets and 2 outlets.

To understand the importance of the problem case, in D4.2 a statistic has been made for the CUS model (12,800 links, 10,500 nodes, 970 km) on the number of T-junctions and their configurations. The first result is that 90% of the T-junctions in the network are represented by 12 geometries of T-junctions and 33% with the diameters 100mm-100mm-100mm. Here after in **Figure 3** and **Figure 4**, statistics are shown for the more representative T-junctions (*i.e.*, the latter case).

There are six configuration possibilities depending on the flow directions that may change for the same T during the day, but this could be reduced to four configurations as shown in **Figure 3**. For each configuration, their percentage of apparition in the network is given at the bottom right. The result is that the configurations 1 and 3 are the most represented in the network. Moreover, imperfect mixing may occur for N-junctions or U-junctions when geometries 1 then 3 are in series.

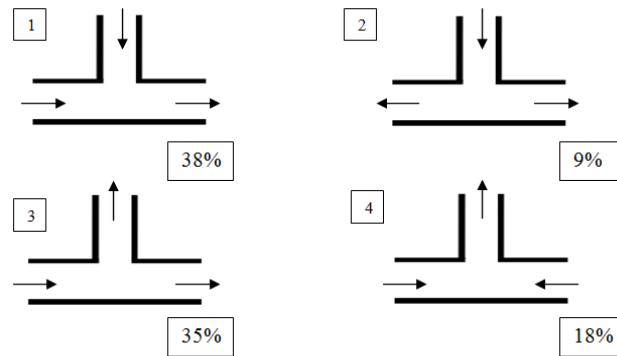


Figure 3: The 4 principal configurations of T-junctions and their repartitions in Strasbourg WDN.

Additionally, a study of the Reynolds number at each input/output was made. The Porteau software has been used for the hydraulic simulation over a day duration with a hydraulic time step of 5 minutes to work out the algebraic Reynolds number shown in **Figure 4**. It is positive if the flow goes into the T-junction, negative otherwise. For a T-junction the branch side has been given the number 3 and the two main branches given a random number 1 or 2. The following graph in **Figure 4** presents a statistical repartition of the Reynolds numbers for the 3 branches. It can be seen that laminar regime occurs for 21% of cases and transitional regime for the other 19% of cases. Then, only 60% of cases correspond to the turbulent flow.

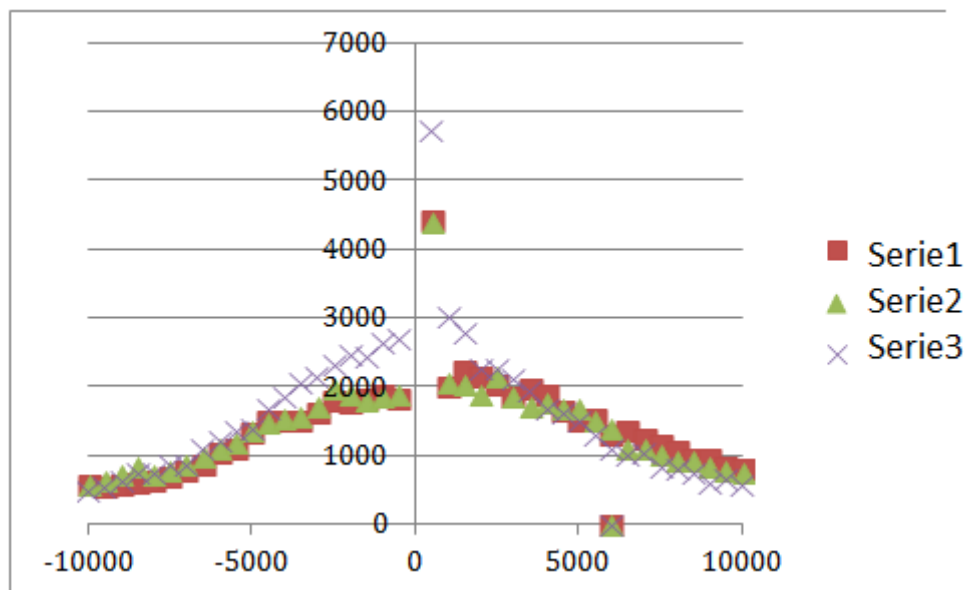


Figure 4: Frequency of Reynolds number for 3x100 T-junction of Strasbourg network.

The aim of this study is to determine a law of imperfect mixing with the help of high CFD simulations. By injecting a tracer through one entry (see **Figure 2**) at inlet In2 of the double T, we want to know how it will spread into the outputs depending on the velocities as well as the distance L between the double T. In the simulation we put no contaminant for the inlet 1 and full concentration for the inlet 2.

Two comparable meshes are used. One was made with ANSYS Fluent [8] with a cut-cell algorithm and is approximately 800,000 cells. The other was prepared with Salome [9] and is a structured mesh of more or less 1,000,000 cells. Both have been tested for grid convergence on the cases where all inflows and outflows are the same and comparative results were found.

We divided the work in two parts depending on our materials. Internally, we have access to a calculation centre with 40 licenses for Fluent [8]. We have also been able to use the calculation centre of Aquitaine (France) called MCIA [10] with more resources but without any ANSYS/Fluent licenses. Therefore laminar calculations have been performed by DNS with Code Saturne [11] on the MCIA while the turbulent calculations have been made on the internal calculation centre with Fluent. Moreover additional simulations were made with a very fine mesh on the cluster of the CINES [12] to test the mesh convergence for the turbulent cases.

Conclusion:

The problem of imperfect mixing has been studied in the case of cross junctions [1; 2]. The double T-junction case has also been studied [2] and a complement of it is proposed in this study. It has been chosen to perform CFD simulations in laminar and turbulent cases as well as experimentations. Both of them will then be compared to permit the implementation of a 1D law for imperfect mixing.

2. Kriging Interpolation

For making multi-dimensional inference, we use in this research the well-known Kriging method or Gaussian Process Regression [13] in geological sciences. This is a minimum variance method based on the definition of a probability distribution at each of the n sample points x_i . In this study the library DACE [14] was first tested in Matlab, but it was preferred to implement the overall method to improve flexibility.

The method chosen is the universal Kriging that we detail below. It consists of two steps.

Step 1- Regression model and maximum-likelihood parameter estimation

Considering n points of observation s_1, s_2, \dots, s_n . The function is taken as the sum of a polynomial function of s and a stochastic scalar function $Y(s)$.

$$Z(s) = Y(s) + \sum_{l=1}^p f_l(s)\beta_l \quad (3)$$

With β_1 the unknown coefficient of the polynomial.

We set

$$F(s) = (f_1(s), \dots, f_p(s)) \text{ and } \beta(s) = \begin{pmatrix} \beta_1 \\ \vdots \\ \beta_p \end{pmatrix}$$

Therefore

$$Z(s) = Y(s) + F(s)\beta$$

Remark: if the row-vector $F(s)$ is only composed of one element equal to 1, the method is called ordinary Kriging, otherwise it is universal Kriging.

It is also supposed that the stochastic part is of expectation zero.

$$E(Y(s)) = 0$$

It implies:

$$\begin{aligned} Cov(Z) &= Cov(Y) = E[YY^T] \\ E[Z(s)] &= F(s)\beta \end{aligned}$$

With Z and Y are the column n -vector with components $(Z(s_i))$ and $(Y(s_i))$

Finally the covariance is set as:

$$\begin{aligned} K &= Cov(Y) = \sigma^2 R(Y) \\ R(Y(s_i), Y(s_j)) &= \prod_{k=1}^m \exp(-\theta_k |s_{ik} - s_{jk}|^{\gamma_k}) \end{aligned} \quad (4)$$

Where m is the dimension of the problem (here 4) and θ_k and γ_k are to be estimated. The same equation is used when calculating $R(Y(s_0), Y(s_j))$ with the coordinates of the estimation point s_0 instead of any observation point s_i .

It is supposed that the probability density function associated to Y on the sample points s_1, s_2, \dots, s_n is a multidimensional Gaussian:

$$\frac{1}{(2\pi)^{\frac{n}{2}} \det(K)^{\frac{1}{2}}} e^{-\frac{1}{2}(Z-F\beta)^T K^{-1} (Z-F\beta)} \quad (5)$$

With

$$K = (K_{ij})_{i,j \in [1,n]}, Z = (Z(s_i))_{i \in [1,n]}, \text{ et } F = (F_{il})_{i \in [1,n], l \in [1,p]}$$

The Y pdf can be rewritten as:

$$\frac{1}{(2\pi\sigma^2)^{\frac{n}{2}} \det(R)^{\frac{1}{2}}} e^{-\frac{1}{2\sigma^2}(Z-F\beta)^T R^{-1} (Z-F\beta)}$$

With

$$R = (R(Y(s_i), Y(s_j)))_{i,j \in [1,n]}$$

$\sigma, \beta, \theta_k, \gamma_k$ ($k \in [1, m]$) are estimated with the help of a maximum likelihood optimisation. The function log-likelihood to minimise is:

$$f(\sigma, \beta, \theta_k, \gamma_k) = \frac{n}{2} \log(2\pi\sigma^2) + \frac{1}{2} \log(\det(R)) + \frac{1}{2\sigma^2} (Z - F\beta)^T R^{-1} (Z - F\beta) \quad (6)$$

The function f is differentiated with respect to σ and β to derive necessary optimality condition by cancelling the gradient function:

$$\frac{\partial f(\sigma, \beta, \theta_k, \gamma_k)}{\partial \sigma} = \frac{n}{\sigma} - \frac{1}{\sigma^3} (Z - F\beta)^T R^{-1} (Z - F\beta)$$

Therefore

$$\frac{\partial f(\sigma, \beta, \theta_k, \gamma_k)}{\partial \sigma} = 0 \Rightarrow \hat{\sigma}^2 = \frac{1}{n} (Z - F\beta)^T R^{-1} (Z - F\beta) > 0 \quad (7)$$

And

$$\nabla_{\beta} f(\sigma, \beta, \theta_k, \gamma_k) = \frac{1}{2\sigma^2} 2F^T R^{-1} (Z - F\beta) \text{ Then}$$

$$\frac{\partial f(\sigma, \beta, \theta_k, \gamma_k)}{\partial \beta} = 0 \Rightarrow \hat{\beta} = (F^T R^{-1} F)^{-1} F^T R^{-1} Z \quad (8)$$

The gradients of function f with respect to θ_k and γ_k are given by:

$$\frac{\partial f(\sigma, \beta, \theta_k, \gamma_k)}{\partial \theta_k} = \frac{1}{2} \text{tr}(R^{-1} [R \circ D_k]) - \frac{1}{2\sigma^2} (Z - F\beta)^T R^{-1} [R \circ D_k] (Z - F\beta) \quad (9)$$

Where tr is the matrix operator trace;

$$[R \circ D_k]_{ij} = R_{ij} \times (D_k)_{ij}$$

with \circ the product of Hadamard; and

$$(D_k)_{ij} = -|s_{ik} - s_{jk}|^{\gamma_k}$$

$$\frac{\partial f(\sigma, \beta, \theta_k, \gamma_k)}{\partial \gamma_k} = \frac{1}{2} \text{tr}(R^{-1}[R \circ E_k]) - \frac{1}{2\sigma^2} (Z - F\beta)^T R^{-1}[R \circ E_k](Z - F\beta) \quad (10)$$

Where

$$(E_k)_{ij} = -\theta_k \log(|s_{ik} - s_{jk}|) |s_{ik} - s_{jk}|^{\gamma_k}$$

Finally $\sigma, \beta, \theta_k, \gamma_k$ are estimated by solving the following minimisation problem:

$$\begin{cases} \min f(\sigma, \beta, \theta_k, \gamma_k) = \frac{n}{2} \log(2\pi\sigma^2) + \frac{1}{2} \log(\det(R(\theta, \gamma))) + \frac{1}{2\sigma^2} (Z - F\beta)^T R(\theta, \gamma)^{-1} (Z - F\beta) \\ \sigma \in \mathbb{R}^+, \beta \in \mathbb{R}^{+p}, \theta \in \mathbb{R}^{+m}, \gamma \in \mathbb{R}^{+m} \end{cases} \quad (11)$$

Where σ, β are taken as optimal value **Eqs. (7) and (8)** for initial values and (θ_k, γ_k) initial values are arbitrary.

It is solved using the Matlab function `fminunc` which permits finding the minimum of an unconstrained multivariable function. As the problem is not strictly convex, σ, β are taken as optimal, value, γ_k components have all been fixed to 1 and the θ_k have been expressed with regards to a non-dimensional parameter scaled by the maximum distance in all four directions.

$$\theta_k = \tilde{\theta} / \max(|s_{ik} - s_{jk}|)^{\gamma_k} \quad (12)$$

With $\tilde{\theta}$ the non-dimensional parameter.

However in this case, and taking into account the observations collected, the objective function may be not defined (see **Figure 5**), due to the correlation matrix R for small θ , which is not an invertible matrix. Therefore a regularisation term is added to the diagonal of the correlation matrix R :

$$R_\alpha = R + \alpha I_n$$

With α the regularisation term. This is equivalent to making a ridge regression or using a Tikhonov regularisation technique, it is also called nugget effect.

The new problem to solve becomes:

$$\begin{cases} \min f(\sigma, \beta, \tilde{\theta}) = \frac{n}{2} \log(2\pi\sigma^2) + \frac{1}{2} \log(\det(R_\alpha(\theta))) + \frac{1}{2\sigma^2} (Z - F\beta)^T R_\alpha(\theta)^{-1} (Z - F\beta) \\ \sigma \in \mathbb{R}^+, \beta \in \mathbb{R}^{+p}, \tilde{\theta} > 0, \theta = \tilde{\theta} / \max(|s_{ik} - s_{jk}|)^{\gamma_k} \end{cases} \quad (13)$$

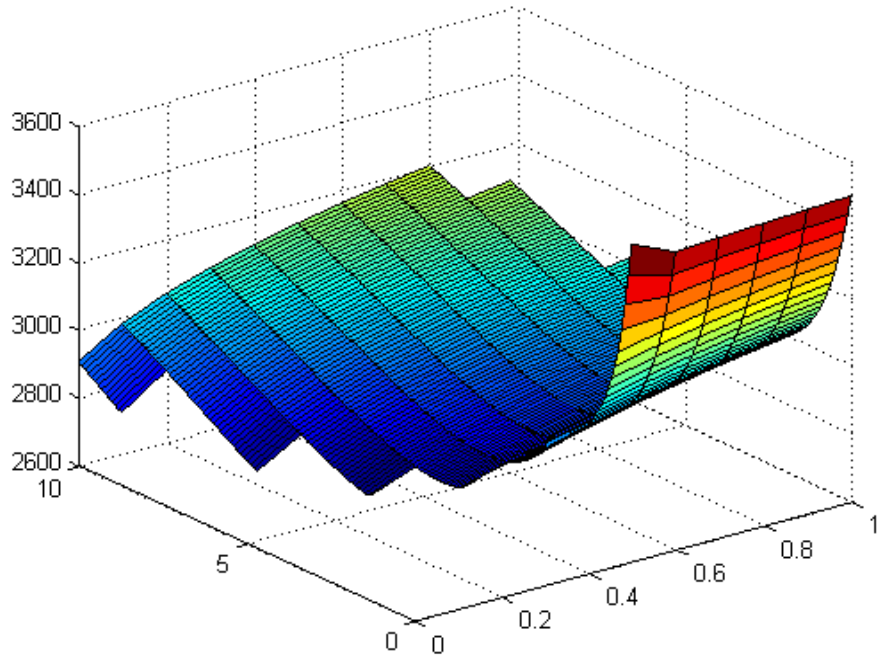


Figure 5: Contour plot of the log-likelihood function with respect to the shape parameter theta and the regularisation parameter.

The **Figure 5** represents the function $f(\tilde{\theta}, \alpha)$ for $\tilde{\theta} \in [0, 10]$ and $\alpha \in [0, 1]$, with σ, β fixed as optimal values **Eqs. (7) and (8)**. There are 3 regions for α . If α is too small (< 0.45), the R matrix may not be invertible (because not regularised enough), therefore its determinant is null and the function f equals $-\infty$. On the other hand, if α is too large (> 0.6), the correlation matrix may be too close to $2I_n$, therefore its determinant is approximately 2^n , the matrix is invertible but its determinant in floating-point arithmetic is $+\infty$. Optimal $\alpha = 0.5$ has been chosen for R to be invertible for the full $\tilde{\theta}$ range. f minimum value is reached for $\tilde{\theta} = 3.128$.

Step 2- Kriging Interpolation

With the maximum-likelihood estimation of parameters σ, β, θ_k it is possible to predict the polynomial term of **Eq. (3)** or regression term. The residual term Y is not a white noise, it is possible to reduce it further by explaining the maximum of the intragroup variance.

An estimation of Z at the point s_0 is taken as a linear combination of Z from the observation points.

$$\hat{Z}(s_0) = \sum_i \lambda_i(s_0) Z(s_i) \quad (14)$$

Where the λ_i are the unknowns of the problem.

Moreover we consider an unbiased predictor:

$$E[\hat{Z}(s_0)] = E[Z(s_0)]$$

This leads to:

$$\forall s_0, \sum_i \lambda_i F(s_i) \beta = F(s_0) \beta$$

Which is satisfied if

$$\forall l \in [1, p], \sum_i \lambda_i f_l(s_i) = f_l(s_0)$$

We seek λ_i that minimises the variance of the error term:

$$\min e(\lambda) = \text{Var}[\hat{Z}(s_0) - Z(s_0)]$$

By expanding the error term

$$\begin{aligned} \hat{Z}(s_0) - Z(s_0) &= \sum_i \lambda_i (Y(s_i) + F(s_i) \beta) - Y(s_0) - F(s_0) \beta \\ &= \sum_i \lambda_i Y(s_i) - Y(s_0) \end{aligned}$$

It follows

$$\begin{aligned} \text{Var}[\hat{Z}(s_0) - Z(s_0)] &= \text{Var} \left[\sum_i \lambda_i Y(s_i) - Y(s_0) \right] \\ &= E \left[\left(\sum_i \lambda_i Y(s_i) - Y(s_0) \right)^2 \right] - \left(E \left[\sum_i \lambda_i Y(s_i) - Y(s_0) \right] \right)^2 \\ &= E \left[\left(\sum_i \lambda_i Y(s_i) - Y(s_0) \right)^2 \right] \\ &= E \left[\left(\sum_i \lambda_i Y(s_i) \right)^2 \right] - 2 \sum_i \lambda_i E[Y(s_i) Y(s_0)] + E[(Y(s_0))^2] \\ &= \sum_i \sum_j \lambda_i \lambda_j \text{Cov}(Y(s_i), Y(s_j)) - 2 \sum_i \lambda_i \text{Cov}(Y(s_i), Y(s_0)) \\ &\quad + \text{Var}(Y(s_0), Y(s_0)) \end{aligned}$$

We recall that

$$K_{ij} = \text{Cov}(Y(s_i), Y(s_j))$$

We have found the function to minimise is quadratic in lambda with Hessian K that is symmetrical definite positive (under mild conditions on θ). It is therefore strongly convex.

The convex minimisation problem states:

$$\begin{cases} \min Var[\hat{Z}(s_0) - Z(s_0)] \\ \forall l \in [1, p], \sum_i \lambda_i f_l(s_i) = f_l(s_0) \end{cases} \quad (15)$$

It is possible to define a problem without constraint by defining the Lagrangian function and the Lagrange multipliers μ_l such that:

$$L(\lambda_i, \mu_l) = \sum_i \sum_j \lambda_i \lambda_j K_{ij} - 2 \sum_i \lambda_i k_i(s_0) + k_{00} + 2 \sum_l \mu_l \left(\sum_i \lambda_i f_l(s_i) - f_l(s_0) \right) \quad (16)$$

Or

$$L(\lambda_i, \mu_l) = \langle \lambda | K \lambda \rangle - 2 \langle \lambda | k(s_0) \rangle + \sigma^2 + 2 \left\langle \mu \left| \sum_i \lambda_i f(s_i) - f(s_0) \right. \right\rangle$$

With $k_i(s_0) = \text{Cov}(Y(s_0), Y(s_i))$ and $k_{00} = \text{Cov}(Y(s_0), Y(s_0)) = \sigma^2$ are given by **Eq. (4)**.

The sufficient and necessary optimality conditions are:

$$\begin{cases} \forall l \in [1, p], \sum_i \hat{\lambda}_i f_l(s_i) = f_l(s_0) \\ \forall i \in [1 \dots n], \sum_j \hat{\lambda}_j K_{ij} - k_i(s_0) + \sum_l \hat{\mu}_l f_l(s_i) = 0 \end{cases} \quad (17)$$

These last equations can be written as the saddle point equation:

$$\begin{pmatrix} K & F \\ F^T & 0 \end{pmatrix} * \begin{pmatrix} \hat{\lambda} \\ \hat{\mu} \end{pmatrix} = \begin{pmatrix} K_0 \\ F(s_0)^T \end{pmatrix} \quad (18)$$

Using the Schur complement of K in the full matrix, it leads to the expression of optimal λ and μ :

$$\begin{aligned} \hat{\mu} &= \left[F^T K^{-1} F \right]^{-1} \left(F^T K^{-1} K_0 - F(s_0)^T \right) \\ \hat{\lambda} &= K^{-1} \left(K_0 - F \hat{\mu} \right) \end{aligned}$$

Moreover we also obtain an estimation of the error variance by using **Eq. (17)** in the **Eq. (16)**:

$$Var[\hat{Z}(s_0) - Z(s_0)] = \hat{\sigma}^2 - \hat{\lambda} K_0 - \hat{\lambda}^T F \hat{\mu} \quad (19)$$

Conclusion:

The Kriging interpolation consists of two parts: The first one comes back to estimate the parameters σ , β , θ_k at maximum-likelihood sense; the γ_k are fixed to 1s; a regularisation term, α is added to the diagonal of the correlation matrix. Finally an optimisation problem is solved to find the parameters. The second part consists of a weighted sum of the observations. It gives an effective way of interpolating non-structured points.

3. Design of experiments and Delaunay Triangulation

It was determined in previous study [2] that for $Re > 10,000$, no further change in behaviour is observed. Additionally, it has been shown by [2] that after 20 diameters for the length between 2 Ts, complete mixing occurs. A discussion with operating partners of SMaRT-OnlineWDN has permitted fixing the low boundary for distance between Ts. Indeed, crosses and double T-junctions can't be compared easily because some space is needed to put in a valve in most cases. Therefore we have chosen the domain for the parameters of the **Table 1**.

Table 1: Parameter domain

Factors	Low level (-)	Mid level chosen	High level (+)
Reynolds average	1 000	5 000	10 000
Distance inter-T	5*Diameters	10* Diameters	20* Diameters
Fraction Reynolds entry 1	0	50	100
Fraction Reynolds output 1	0	50	100

To complete the study, we chose to make at least three experiments for every factor; as CPU time is long to get the stability, 81 simulations have been carried out. Additionally, we take advantage of control point simulation to get more reliable results in concordance with the Kriging interpolation and Delaunay triangulation.

DNS and LES simulations are computationally demanding, therefore a method is needed to find the best point of simulation. One well-known method is the Latin-Square design consisting of dividing the space into a fixed number of squares and then randomly picking points in each square. However, for computational simulation, it has the drawback of needing a lot of simulation points and it is not optimal to improve the interpolation fitting.

In this study we have selected the Delaunay triangulation method. This method has been used for the FFAST project [15] to improve a domain-decomposition. It was made to enrich the database of principal components analysis basis functions used in oscillating airfoils in a compressible flow context.

The Delaunay triangulation method is usually used for space partitioning. It defines a list of triangles from a list of points where no point are strictly inside any circumcircle of any triangle. Here it is used to determine new points of simulations by a greedy algorithm:

- For each point of the design plan, calculate the difference between its value and the interpolated value at that point if it is not taken into account;
- For every Delaunay triangle calculate the sum of the error of its vertices multiplied by its area, vertices being the points of the design plan;
- The best point candidates to include in the design plan are the centres of gravity for triangles with the highest weight; then, in this research, the selected point is the closest point with rounded coordinates, more convenient for simulation.

A simple example is given in **Figure 6** taking into account 9 points, which are given in **Table 2**. The function M is the list of the measurements and E is the list of error of interpolation when discarding the point.

Table 2: Example Delaunay method with associated errors.

$M(x,y)$	$x = 0$	$x = 1$	$x = 2$
$y = 2$	3	3	3
$y = 1$	2	2	2
$y = 0$	1	0	1

$E(x,y)$	$x = 0$	$x = 1$	$x = 2$
$y = 2$	0.70	0.48	0.70
$y = 1$	0.57	0.53	0.57
$y = 0$	1.75	1	1.75

The method divides the space in eight triangles of equal area. The maximum error is found on the points (0,0) and (0,2) equal to 1.75. In this case, the two-bottom triangles will most likely be chosen for new simulations (blue cross). The method detects the point most problematic, here the only point not in the plan $z=y+1$, and refines around it.

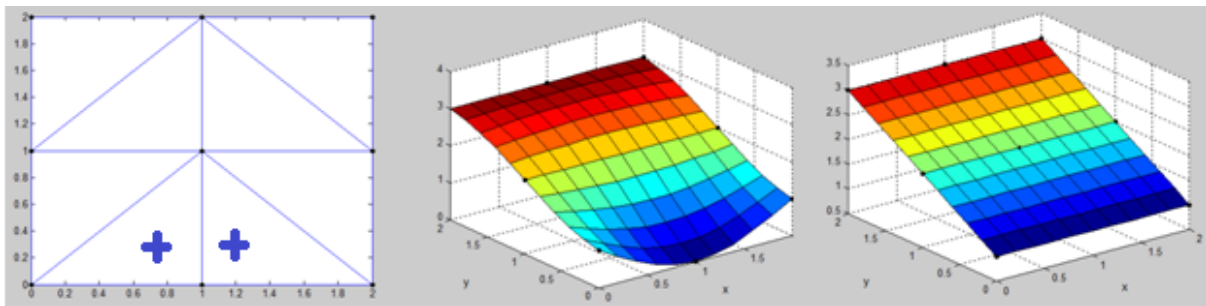


Figure 6: left) Delaunay triangle; center) interpolation full; right) interpolation without point (1,0)

The imperfect mixing law is computed from **Table 3** of results of the simulations. The Kriging method is used to interpolate any value inside the range. Extrapolation out of range is not recommended and more research needs to be carried out there.

Table 3 gives a non-exhaustive list of the simulations performed. The first column is the distance between Ts (in diameters), the second is the average Reynolds number (in the centre of the pipe), the third column is the Reynolds percentage of inlet 1 (straight inlet see Fig. 1) from the previous one, the fourth is for the outlet 1 (%In2 and %Out2 can be found from $100 - \%In1$ and $100 - \%Out1$ respectively). The last two columns give the repartition of contaminant for outlet 1 and 2 averaged in time.

Indeed LES and DNS simulations are transient and therefore results need to be averaged for a sufficient period of time (*e.g.*, several dozen of minutes) when converged (*cf* **Figure 7**).

For the interpretation of results, it is worth to recall that 100% of the contaminant comes from inlet 2 and 0% from inlet 1. One way of viewing Table 2 is by fixing two parameters and plotting the result with the two others remaining. In Figure 8 the distance is fixed to 5D and the Reynolds number is 1,000. It shows the difference from the complete mixing plan ($Z=\%Out1$) to the result found in the simulations. Therefore the values are inside the boundary space $[0-\%Out1; 100-\%Out1]$. The difference is up to 30%, and therefore can't be neglected. It can also be seen that for $\%In1 < 50$, that is when the straight inlet is dominated, the mixing law is more or less complete. A peak is visible with its top around $\%In1=70$ found in every configuration.

Table 3: Results for simulation CFD (non exhaustive) .

Distance (in diameter s)	Reynolds	%In 1	%Out 1	%ave Out1	%ave Out2
5	1000	20	20	21.6	78.4
5	1000	20	80	81.1	18.9
5	1000	80	20	54.8	45.2
5	1000	80	80	86.3	13.7
5	1000	30	30	30.1	69.9
5	1000	30	70	71.7	28.3
5	1000	70	30	58.8	41.2
5	1000	70	70	93.4	6.6
10	1000	20	20	21.5	78.5
10	1000	20	80	81.5	18.5
10	1000	30	30	32.5	67.5
10	1000	30	70	70.5	29.5
20	1000	20	20	20	80
20	1000	20	80	80	20
5	5000	20	20	20	80
5	5000	20	80	79	21
5	5000	30	30	29	71
5	5000	30	50	49	51
5	5000	30	70	69	31
5	5000	50	30	37	63

distance (in diameter)	Reynolds	%In 1	%Out 1	%ave Out1	%ave Out2
5	5000	50	50	60	40
5	5000	50	70	80	20
5	5000	70	30	44	56
5	5000	70	50	66	34
5	5000	70	70	82	18
5	10000	50	50	62.5	37.5
5	10000	50	70	82	18
5	10000	50	30	39.4	60.6
5	10000	70	50	69	31
8	5000	30	30	31	69
8	5000	30	50	50	50
8	5000	30	70	70	30
10	5000	0	0	30	70
10	5000	0	0	70	30
10	5000	0	0	40	60
10	5000	0	0	81.5	18.5
10	5000	0	0	64	36
10	5000	0	0	50	50
10	5000	0	0	74	26
10	5000	0	0	34	66

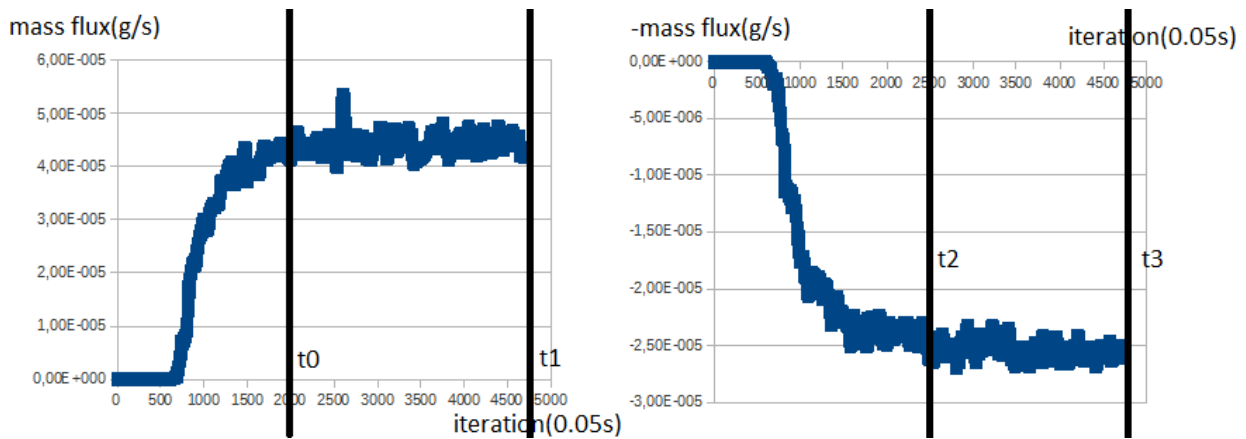


Figure 7: Example of simulation result curve of mass flux (left: Out1, right: Out2).

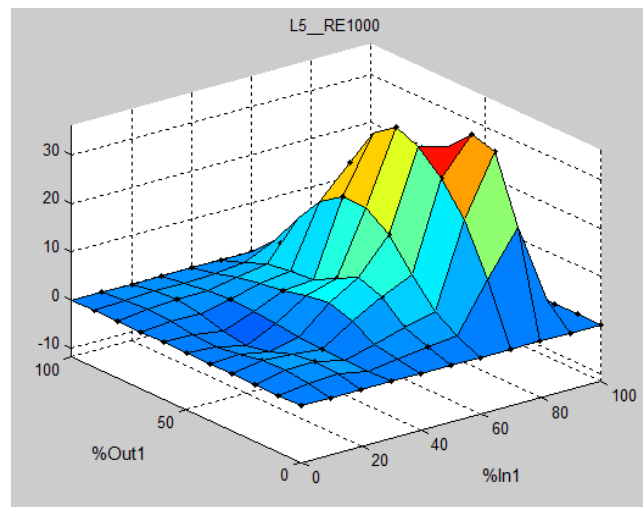


Figure 8: Result for distance = 5D and Reynolds = 1,000.

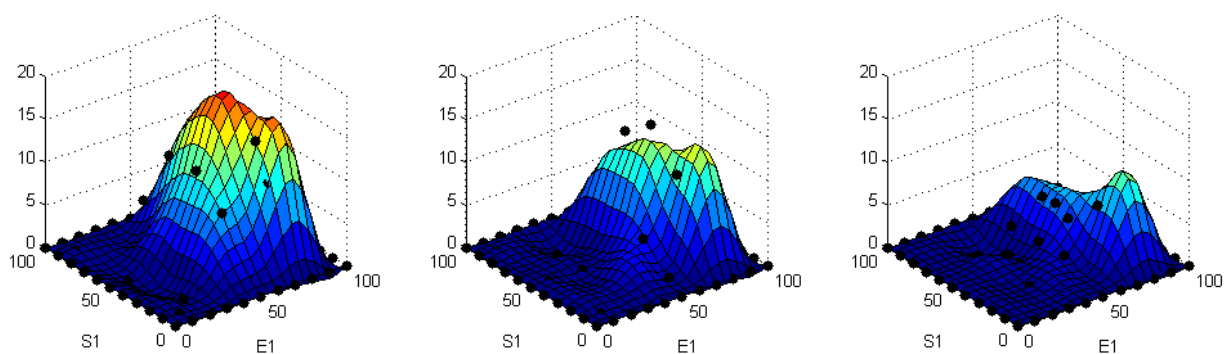


Figure 9: Results for Reynolds = 5000, left) 5D, middle) 8D, right) 10D.

Figure 9 shows the results when the Reynolds number is fixed at 5,000 and the distance is increased from 5D to 10D. It can be observed that there is a peak situated in the right part (when the straight inlet is dominating). The effect on increasing of distance between the two Ts looks to

be a reduction of the peak in height and width. More simulations are needed for the case 5D as well as tests for grid convergence when the straight inlet is dominating ($\%In1 > 80$).

An important issue is the choice of boundary conditions: Contrary to previous studies, the boundary conditions are fixed for the complete mixing case. Indeed a previous study [2] also took these conditions for the left, bottom and top conditions but not for the right boundary condition ($\%In1 = 100$). Around this last one the inlet 2 is almost closed and therefore almost no contaminant enters, however its repartition at the outlet is not clear. The simulations tend to show that it is complete mixing and therefore it was fixed in this study as such.

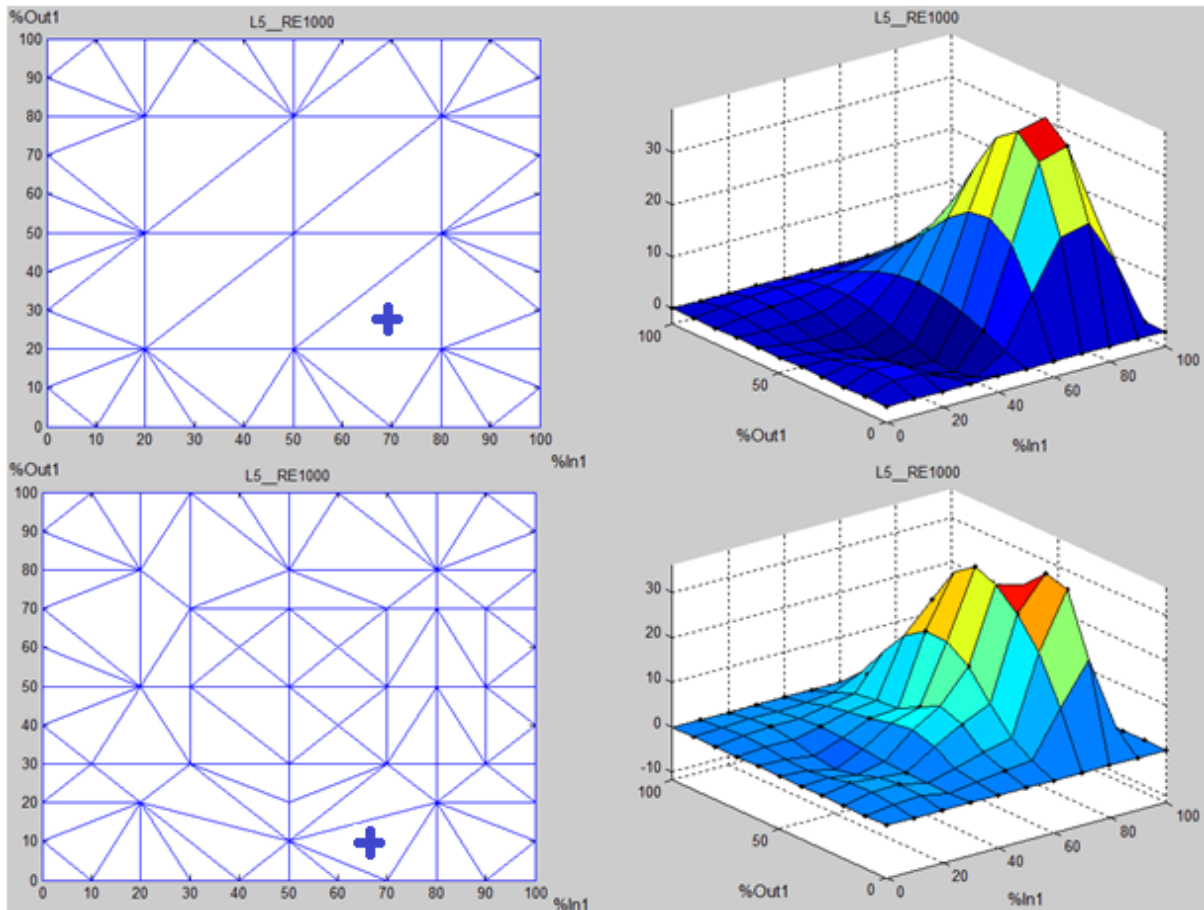


Figure 10: Example of for the distance = 5D, Reynolds = 1,000:
up) before, down) after five simulations chosen by the triangulation of Delaunay.

In the example of **Figure 10**, the Delaunay triangulation method has been applied. On the left can be seen the Delaunay triangles partitioning the domain space, the blue cross define the new point of simulation to make.

Table 4 Table 4 sums up the different new simulation points to consider that were found for the case where distance = 5D and Re = 1,000 are fixed. The first column refers to the order of the simulations made given the Delaunay method and the number 0 is for the initial simulations. The second and third columns give the percentage of inlet 1 Reynolds and outlet 1 Reynolds to the averaged Reynolds number 1,000. Finally the fourth and fifth columns are the absolute errors, either averaged (sum of number of points) or maximum, of all the points simulated at each stage.

In **Table 4**, it can be observed that for both types of error, it is globally decreasing. The error can increase when a particular point is found, in this example (90, 30), but then the Delaunay method will search for points around that will decrease the global error. **Figure 10** on the left shows the points of Delaunay location (vertices of the Delaunay triangle). At the end the method concentrates the points where there is a need for more information, here in the right part, when the straight inlet is dominating.

Table 4: Delaunay points for distance = 5D and Re = 1.000.

Number	%In1	%Out1	Mean. error	max error
1	20	20	13.2	18.7
2	20	80	13.2	18.7
3	50	50	13.2	18.7
4	80	20	13.2	18.7
5	80	80	13.2	18.7
6	50	20	13.2	18.7
7	50	80	13.2	18.7
8	20	50	13.2	18.7
9	80	50	13.2	18.7
1	70	30	11.0	15.6
2	30	30	8.8	14.6
3	60	60	8.3	20.7
4	30	70	7.3	16.4
5	70	70	6.0	18.0

number	%In1	%Out1	Mean. error	max error
6	90	30	8.0	28.3
7	80	30	4.9	27.2
8	90	50	3.3	9.0
9	90	70	2.9	8.2
10	70	50	2.9	9.9
11	50	30	3.7	9.9
12	50	70	2.7	6.4
13	50	10	3.0	6.6
14	40	60	3.0	7.1
15	30	50	2.7	7.1
16	60	40	2.8	6.7
17	80	70	2.4	5.9
18	10	30	2.3	6.0

Conclusion:

The Delaunay method has been used for space partitioning for selecting new CFD simulations to do. At each step, it calculates the absolute interpolation errors, which can be used as a stop criterion. For instance, if we fixed the mean error at 3 as the criteria of convergence, there wouldn't have been a need to continue the simulations after the 18th simulation. It gives an effective way to consume less computational time, by favouring simulations that gives most information.

4. The mesh convergence test

The mesh convergence has been performed on the following points on the MCIA and the CINES High Performance Calculation (HPC) Centres:

Table 5: Mesh convergence tests.

%In1/%Out1	Length (in diameter)	Reynolds number at half-distance	%Out1 (1 000 000 cells)	%Out1 (8 000 000 cells)
50/50	5D	1,000	61.6%	61.8%
80/20	5D	1,000	54.8%	57.3%
80/80	5D	1,000	86.3%	85.0%
70/50	5D	1,000	85.0%	86.0%
70/70	5D	1,000	94.9%	96.3%
50/50	10D	1,000	46.3%	45.2%
90/10	5D	5,000	14.6%	10.3%
80/20	5D	5,000	23.0%	26.7
70/60	5D	5,000	72.5%	75.3%
70/60	10D	5,000	65.0%	76.0%
70/50	5D	30,000	63.5%	65.5%

In **Table 5** the results are shown for different points of simulations when taking 1 million cells and 8 million cells. In the first, second and third columns, a scenario is defined by the proportion of the flow rate entering by inlet 1 and the proportion of outflow leaving by outlet 1, the central length in D, and the Reynolds at the half-distance. Only the case 70(%In1)/60(%Out1), 10D, Re=5,000 is showing an error above 5%. More meshing tests have been needed for this case.

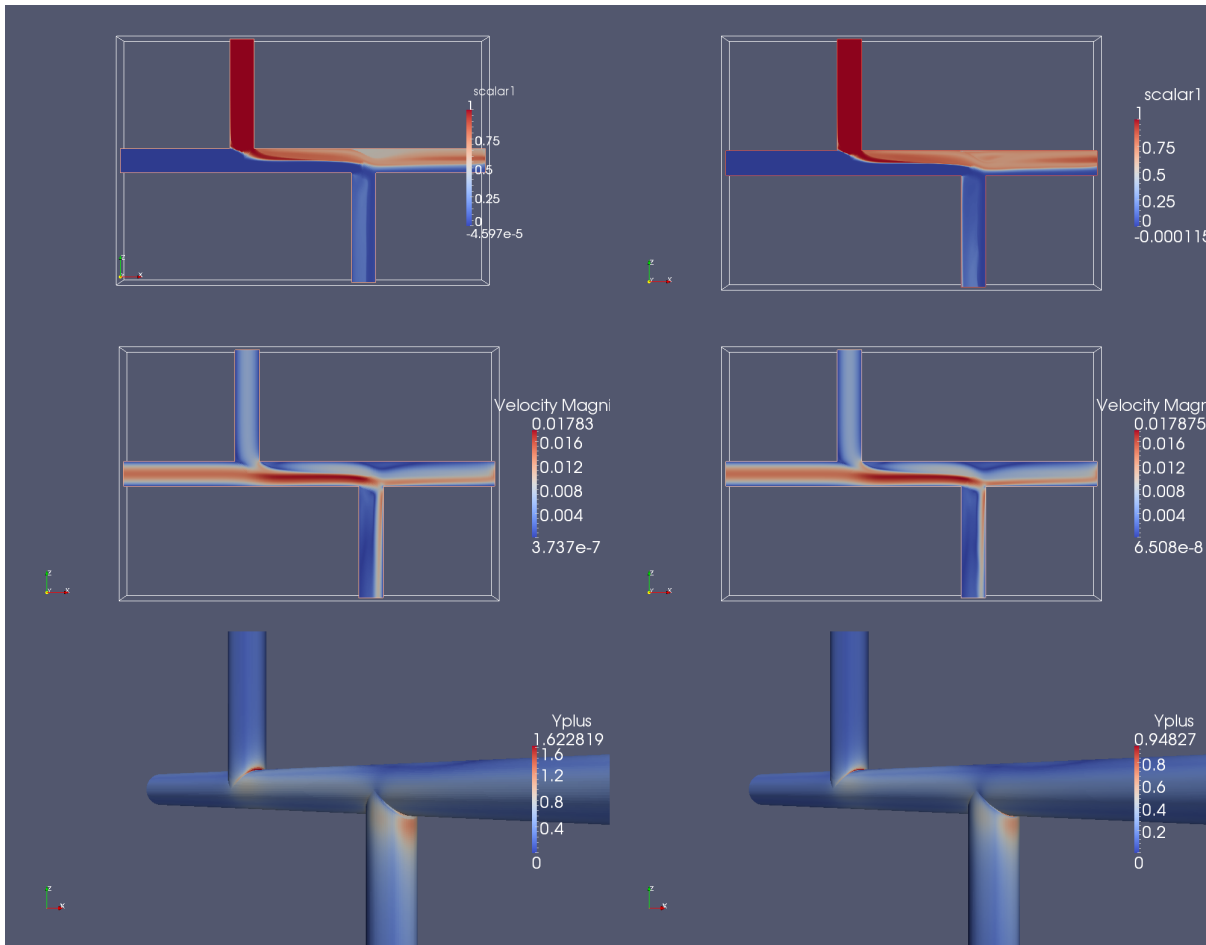


Figure 11: comparison of results between meshes of 1 000 000 and 8 000 000 cells for case Re = 1 000, L = 5D, %In1 = 70; %Out1 = 50. Top) scalar; Middle) velocity magnitude; Bottom) yplus

In Figure 11, the results are shown for the cases 1 million cells and 8 million cells. On top is drawn the passive scalar representing the contamination transported by the fluid (1 is full and 0 means no scalar). The middle of the figure shows the magnitude of the velocity, in this case the velocity coming from inlet In1 is greater than the velocity coming from inlet In2. Finally at the bottom is shown yplus, the non-dimensional wall distance

$$yplus = \frac{u_* y}{\nu}$$

where u_* is the friction velocity at the nearest wall, y is the distance to the nearest wall and ν is the local kinematic viscosity of the fluid. In this case, it is not too big (<5) therefore the law of the wall, the velocity profile at the vicinity of the wall, might be well calculated. In case yplus is not small enough, a remeshing around the biggest value is needed and should be around the corners of the Double T.

Conclusion:

The mesh convergence has been tested on several points of the domain under many scenarios. It shows a difference of less than 5% except for one case. Therefore a mesh of 1 000 000 cells can be used for almost all simulations.

5. CFD Results

All simulation points have been gathered on **Figure 12** below:

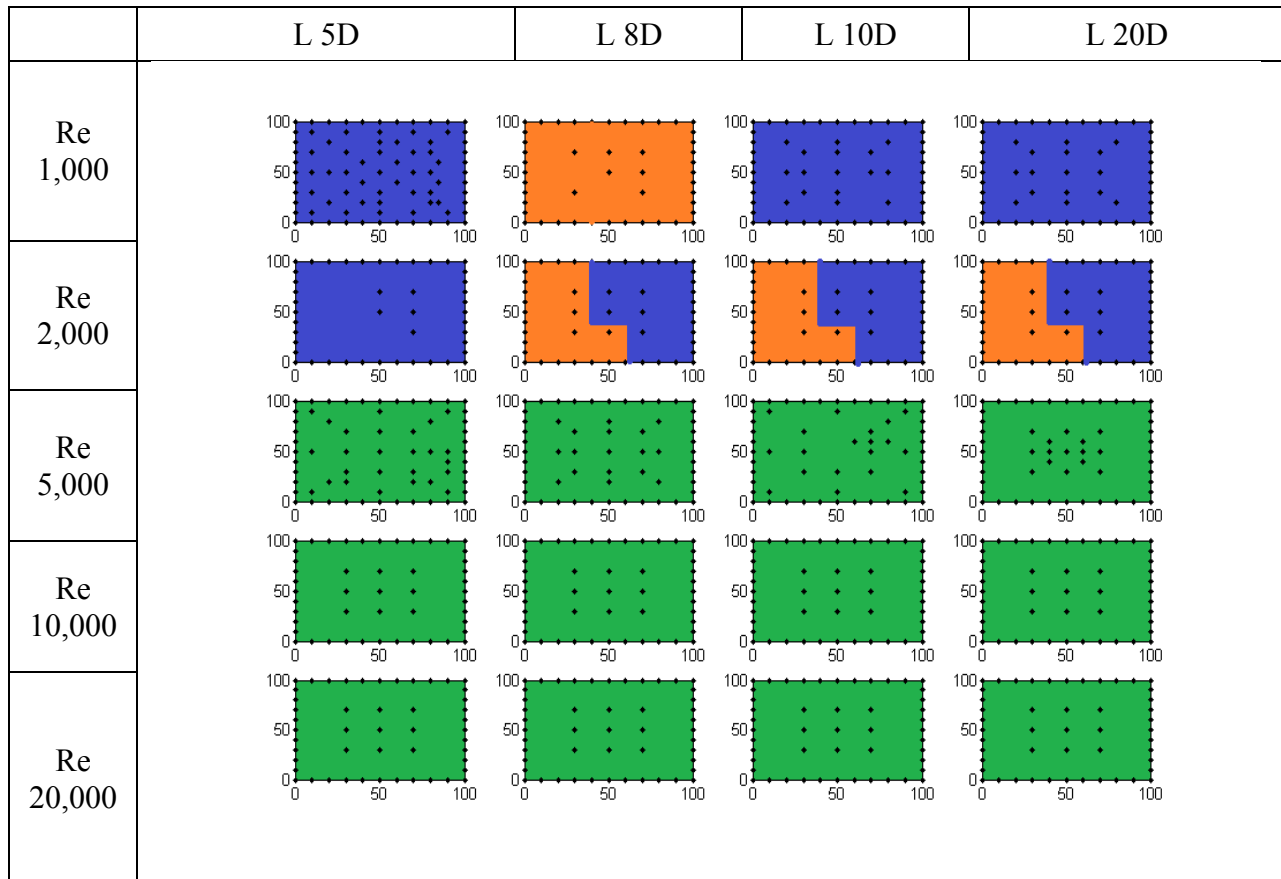


Figure 12: Points of simulations, blue) code Saturne ; orange) code Saturne (two T combined, see part 7) ; green) Fluent.

Figure 12 shows the list of simulations that have been made, here represented by points. Each point is defined by its Reynolds number and its intermediate pipe length as well as its value of %In1 and %Out1 respectively in x-axis and y-axis. The Delaunay method has been mostly used on the space Re1000/LD5 and Re5000/LD5 to ensure the validity of the interpolation.

The results of the 4D interpolation have been drawn on **Figure 13** and **Figure 14**. The first figure gives a lot of information on the behaviour of this law. We may observe that when the second entry is dominating (%In1 < 50%), the mixing is almost perfect. On the other hand when it is the first entry that is dominating, the mixing is not perfect. And it converges toward the perfect mixing with the increase of the distance and the Reynolds number. The cases Re = 30,000, L = 5D, %In1 = 70 was additionally done and is showing that the function converge to a stable equilibrium for high Reynolds number, which may not be the perfect mixing depending on the distance (in case 5D, 70/50 it tends to %Out1=10). It can be seen a slow converging to that state in the laminar case when D increased. **Figure 14** shows that for different configurations of Reynolds fraction in entry and output, the behaviour law is very different. As seen in **Figure 13** when %In1 is lower than 50 the mixing is mostly perfect. In the laminar case the mixing has a clear behaviour, under %In1 = 50 it is perfect mixing and above 70 it is imperfect mixing. In the turbulent case it is more progressive.

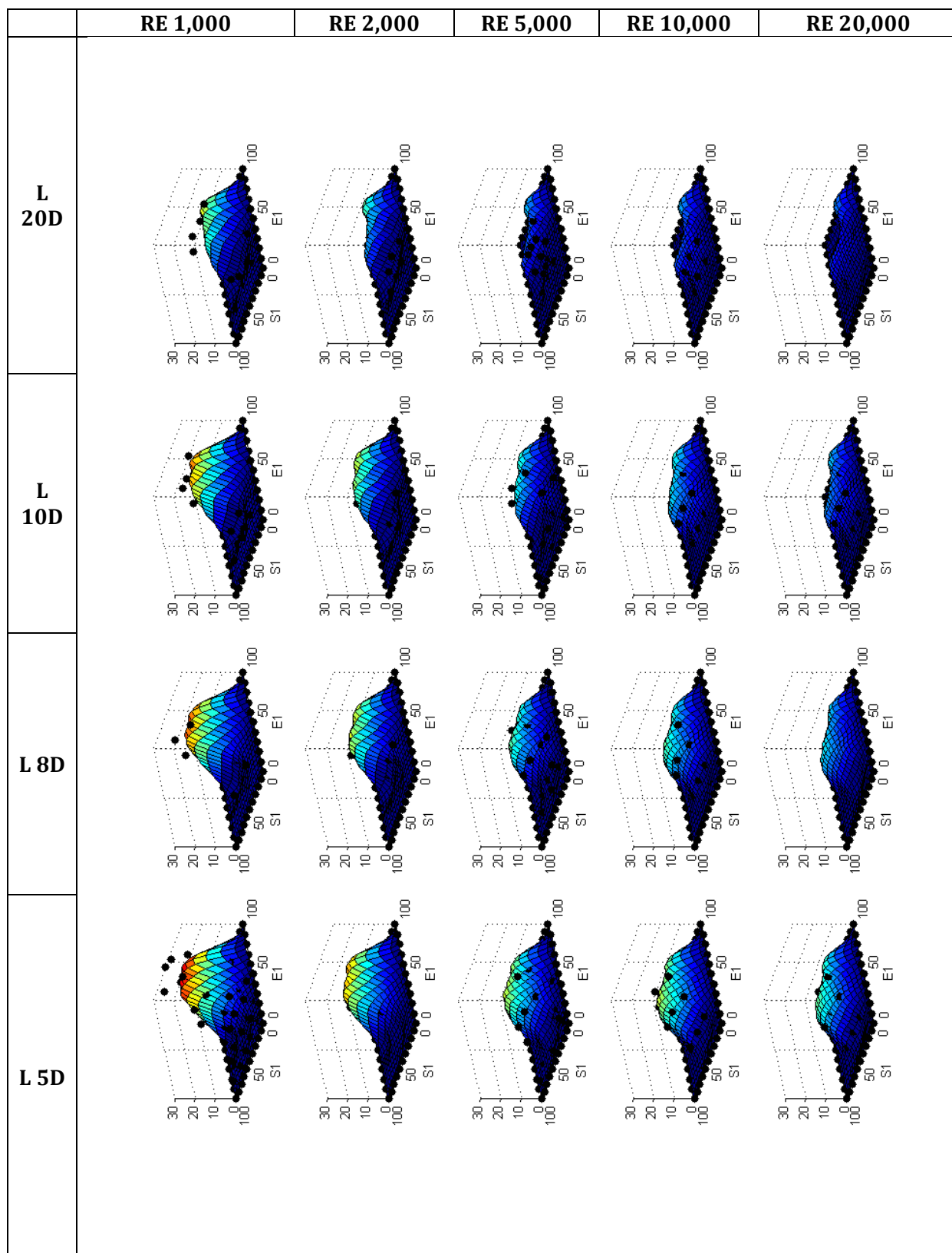


Figure 13: Interpolation 4D Kriging in space %In1 (called E1)/%Out1 (called S1).

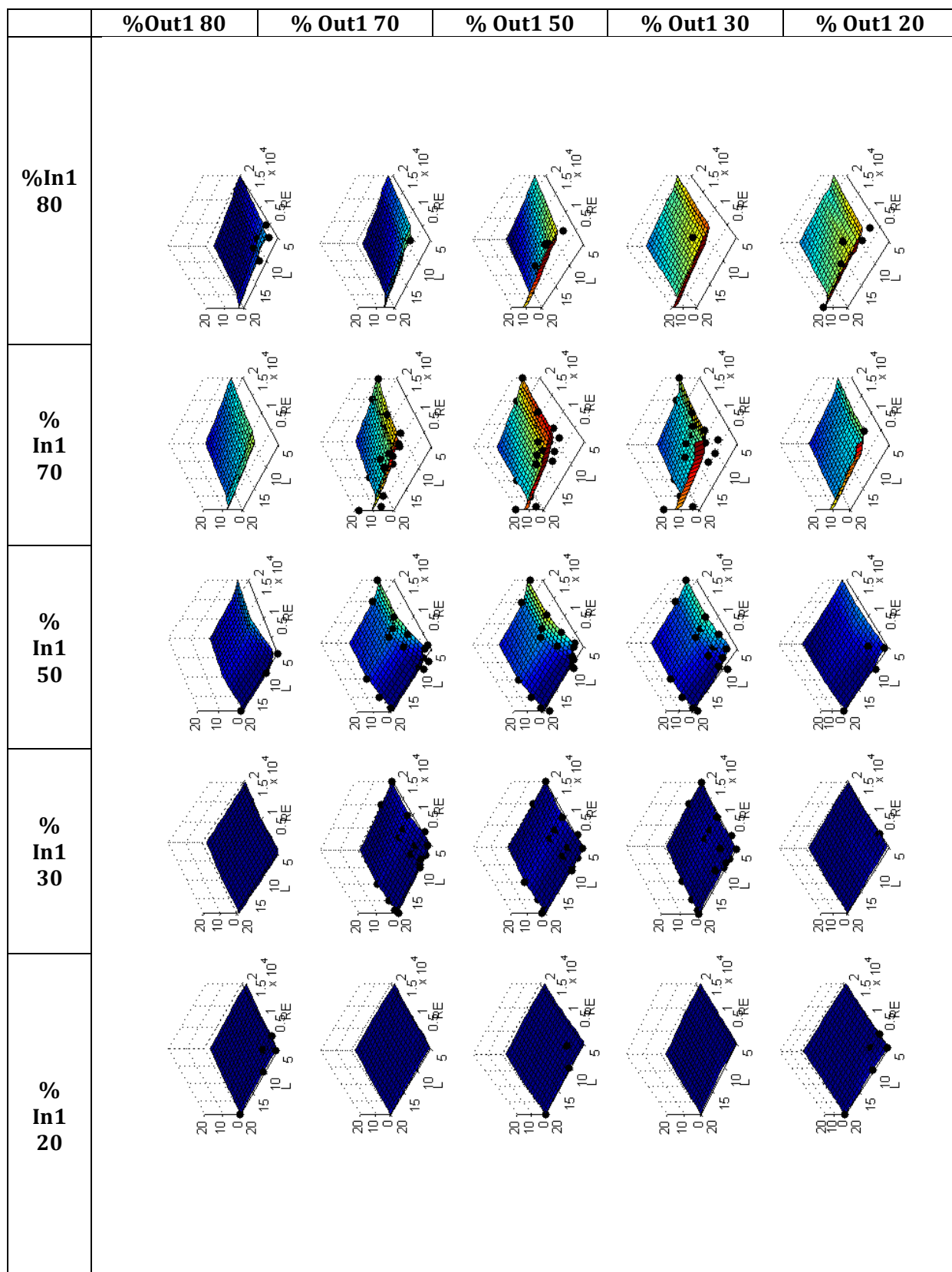


Figure 14: Interpolation 4D Kriging in space L/Re, case %In1 and %Out1 = 20/30/50/70/80.

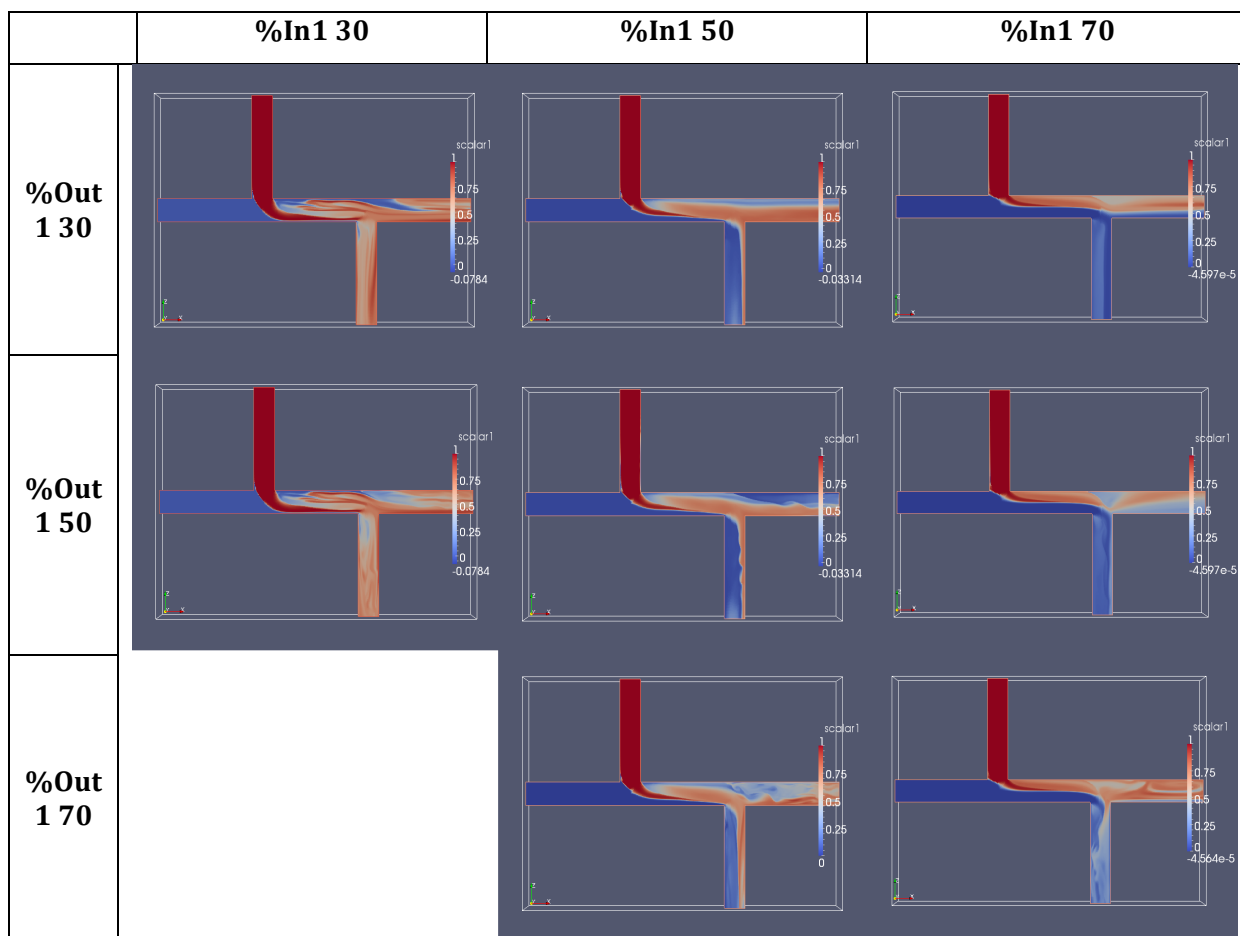


Figure 15: Representation of scalar on longitudinal section of Double T in cases $Re = 1,000$ fixed, $L = 5D$ fixed, and %In1 and %Out1 = 30/50/70

Figure 15 shows the longitudinal section of the double T in the case $Re = 1,000$, $L = 5D$ and %In1 and %Out1 = 30/50/70. It can be seen that when the percentage of inlets at the first entry is lower than for %In1 = 30%, the contaminated water coming from In2 hits the opposite wall, creating turbulence. When %In1 = 50%, the turbulence is caused by the corner of the second T-junction. The more fluid going into the second output, the less stable is the flow. For %In1 = 70, most of the contaminated water goes into the first output regardless of the output velocity repartition.

Conclusion:

More than 250 simulations have been made to describe the phenomena in 4 directions (Reynolds, inter T distance, %In1 and %Out1). The results have been interpolated and projected on two different spaces (%In1, %Out1) and (Re, L). When the first entry is dominated (%In1 < 50) the mixing is perfect. The mixing becomes imperfect when %In1 increases. This behaviour shift is more pronounced for laminar cases whatever the inter T distance, and progressive in turbulent cases. There is a maximum of imperfect mixing around In1% = 70. The mixing tend to the perfect mixing when the inter T distance increases, it is almost perfect for L = 20D in turbulent case. It also decreases when the Reynolds increased but tends to equilibrium that may not be the perfect mixing (tends to 10 when L=5D, %In1=70, %Out1 = 50). The behaviour described can be explained by looking into the longitudinal section of the double T. The mixing is created by hitting the walls, which depends on the ratio of the flows in entry and output.

6. Comparison with the experiments

The test bench pilot is situated in Dresden at the TZW premises. It is shown in **Figure 17**.



Figure 16 : Photo of the pilot in Dresden.

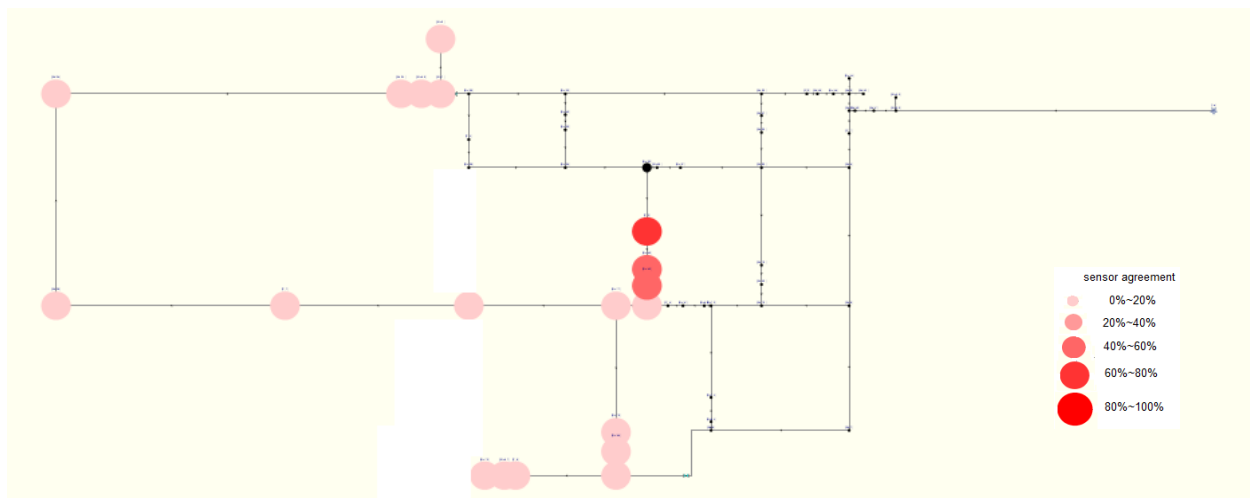


Figure 17: Schema of the pilot in Dresden with a contamination example.

Figure 17 shows an example of contamination in the network of TZW. A contamination is injected at the black point, then the flow brings the contaminated water to a double T junction downstream. The concentration of the fluid is then measured (on the left and bottom of the double_T) at the centre of the tube by a conductivity meter.

A comparison between the simulations and the experiment results has been made. 12 experiment cases have been carried out: $L = 5D, 8D, 10D, 20D$. And for each case the following combinations of Reynolds 30/50/70 have been taken.

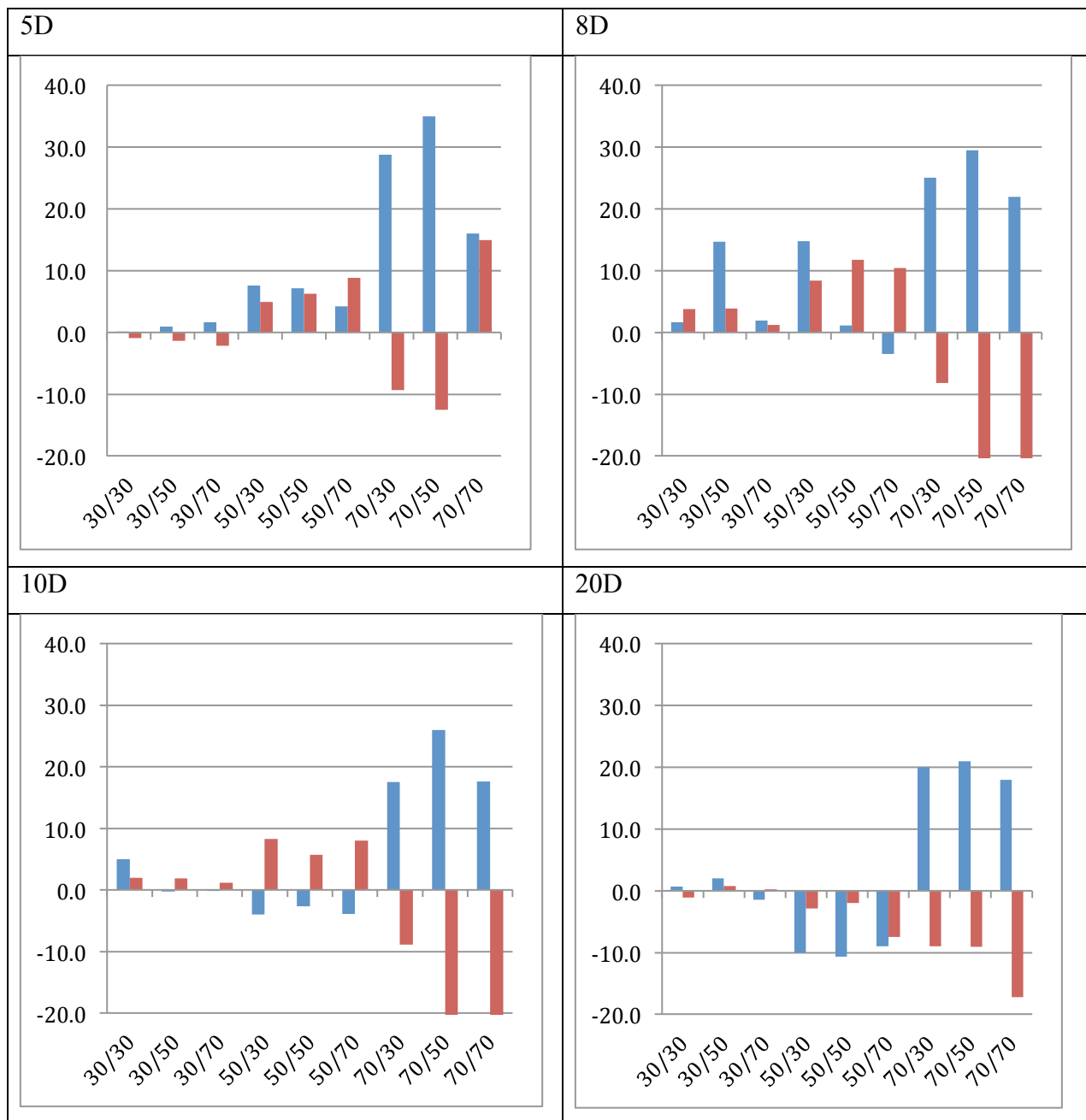


Figure 18: Comparison between CFD and experiments:
 RE = 1,000 (blue CFD simulations, red experiments)

Figure 18 shows the comparisons between simulation and experiments for the laminar case, $Re = 1,000$. The simulations and experiments show big differences in 70/XX cases when the flow going in inlet In1 is at maximum. It might be due to difficulties in keeping a stable low velocity because it is hard to measure. It might be also due to the property of the solution of contaminant. In the laminar case ($Re = 1,000$) the contaminant travels more preferably to the bottom of the tube, the sensor being at the centre of the tube.

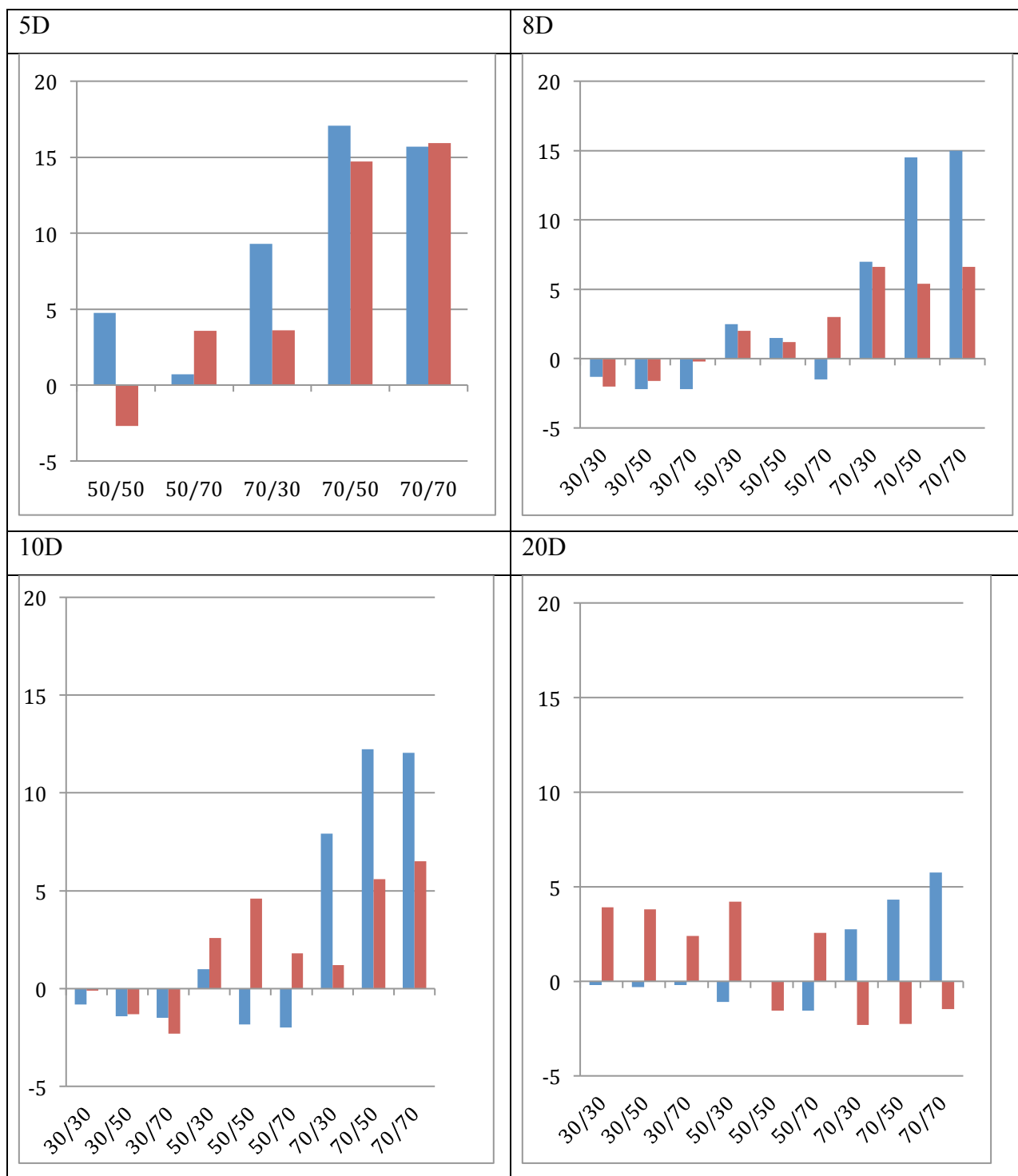


Figure 19: Comparison between CFD and experiments
RE = 2000 (blue CFD simulations, red experiments)

Figure 19 shows better agreement, the trend of simulation and experiment is the same. It is almost perfect mixing when %In1 < 50 and above zero for the cases 70/XX. Larger residues in the last cases may also be due to the contaminant falling slowly to the bottom.

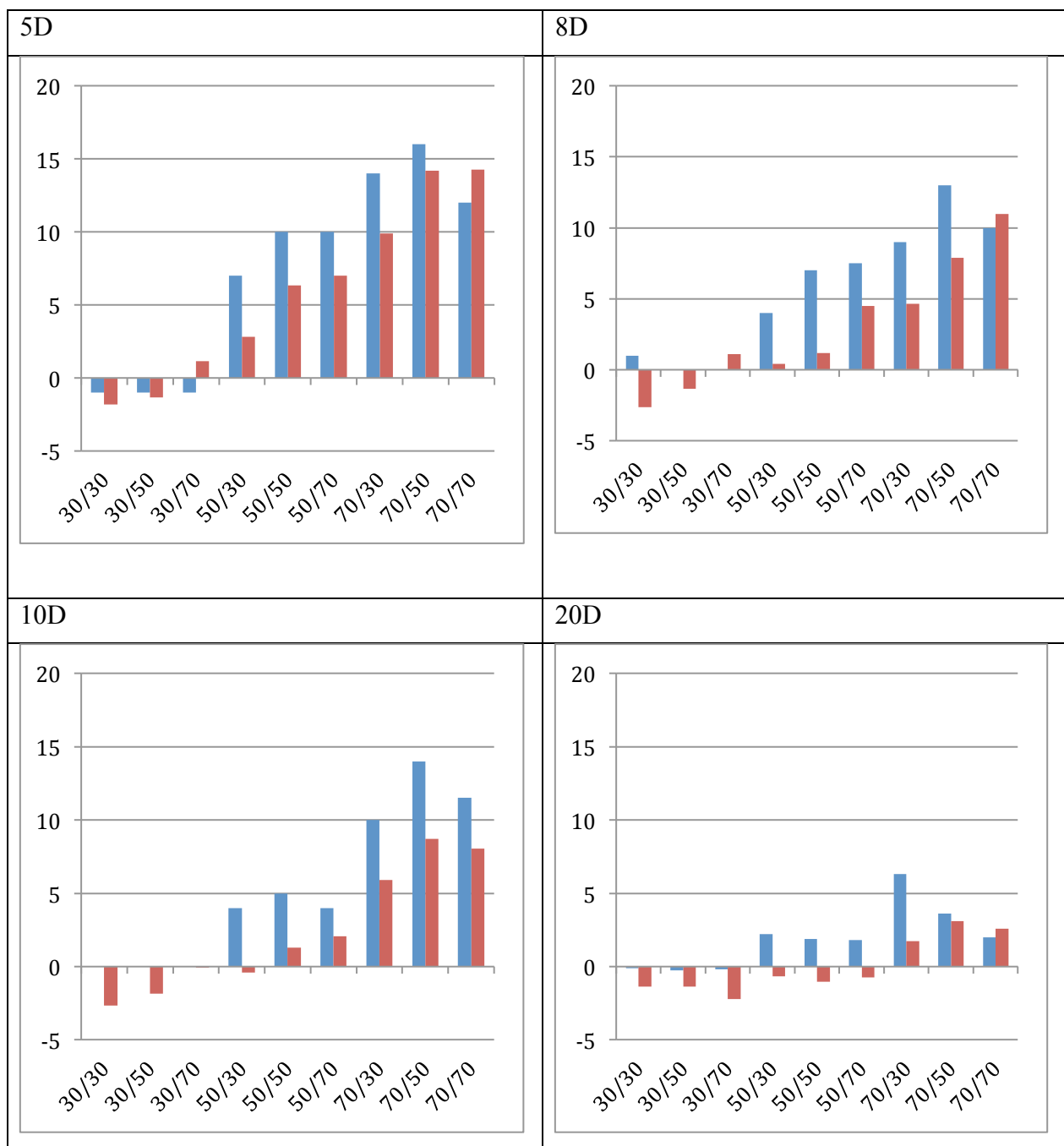


Figure 20: Comparison between CFD and experiments:
RE = 5,000 (blue CFD simulations, red experiments).

Figure 20 shows good matching between CFD simulations and experiments. The difference remaining might also be due to gravity. However as the fluid regime is turbulent, this can be due to the hypotheses of simulation where the effect of turbulence is not enough taken into account.

Conclusion:

The simulations and the experiments show a perfect mixing in the case where entry inlet 1 is dominating;

Some discrepancies between simulation and experimentation can be observed for the case $Re = 1,000$, that may be due to difficulty to measure very low flow in pipes.

A good matching can be seen in the cases $Re = 2,000$ and $Re = 5,000$. The simulations show however an overshooting compared to the experiments and may underestimate the turbulence.

7. Acceleration by combining two single T-junctions

The idea is to combine one single T-junction with another T-junction to treat both as separate, henceforth decreasing the computation time. The idea comes from the study of the simulation result of the double T. We can remark that on **Figure 21** (top left and right), the repartition of the scalar inside the intermediate pipe is the same, and at the bottom only the results at the two outlets are different. The entries are dominating the phenomenon. The idea is then to simulate the behaviour in a long T-junction. Then the scalar and the velocities are taken from a cross-section and re-injected as input in another T-junction representing the outputs.

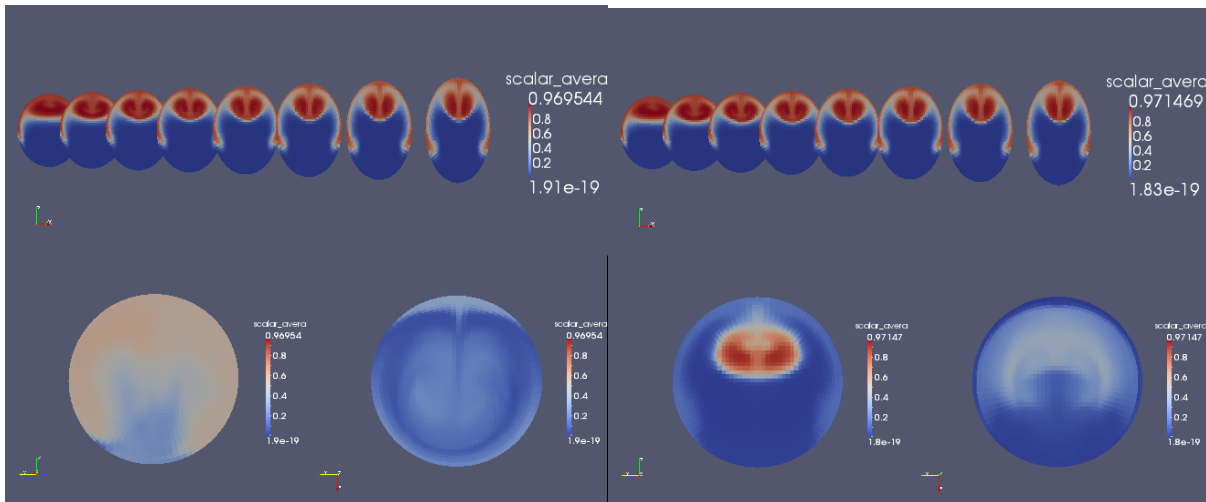


Figure 21: Cross-section in cases 10D, Re=1,000, 80/20 and 80/80

A study on the use of two T-junctions instead of one double T has been made. The method works on the cases Re = 1,000 5D and 10D on most of the points (see **Figure 22** and **Figure 23**). However, the points 70/70 and 70/50 (in 10D case) present a significant error.

It works well for Re = 2,000 cases (**Figure 24**).

Finally, for Re = 5,000 (**Figure 25**) the method shows different results from the double T simulations. In the latter case, more research is needed to conclude on the viability of the method.

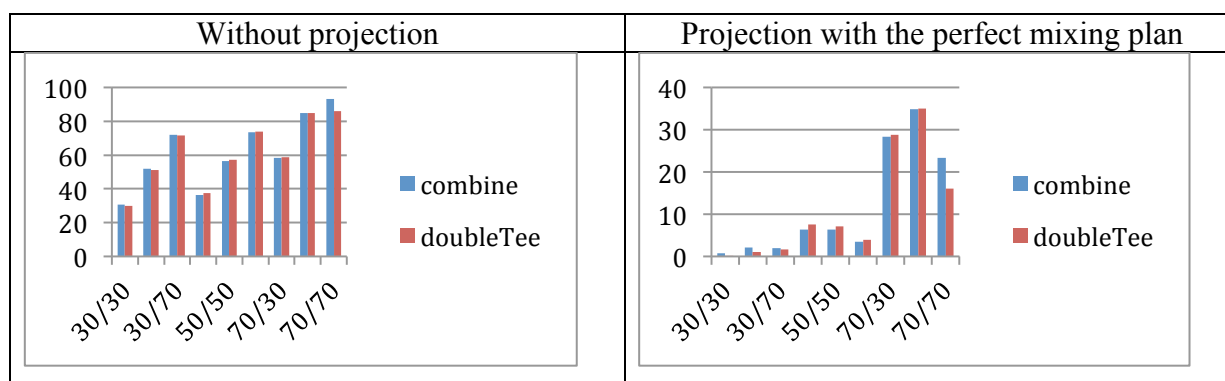


Figure 22: Comparison combined, 5D Re=1,000

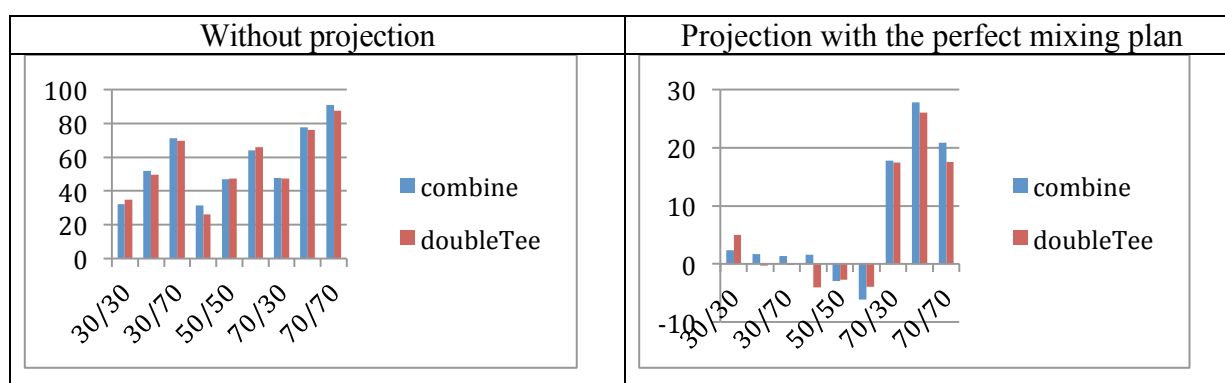


Figure 23: Comparison combined, 10D Re=1,000.

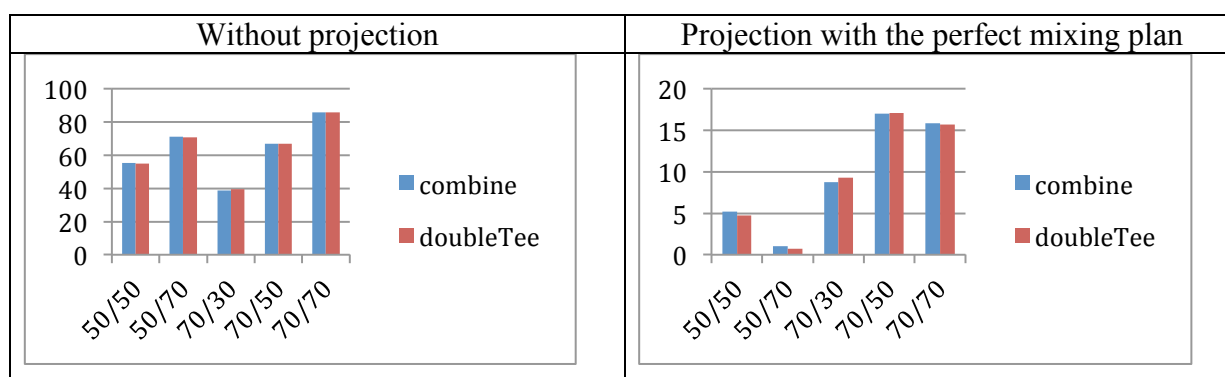


Figure 24: Comparison combined, 5D Re=2,000.

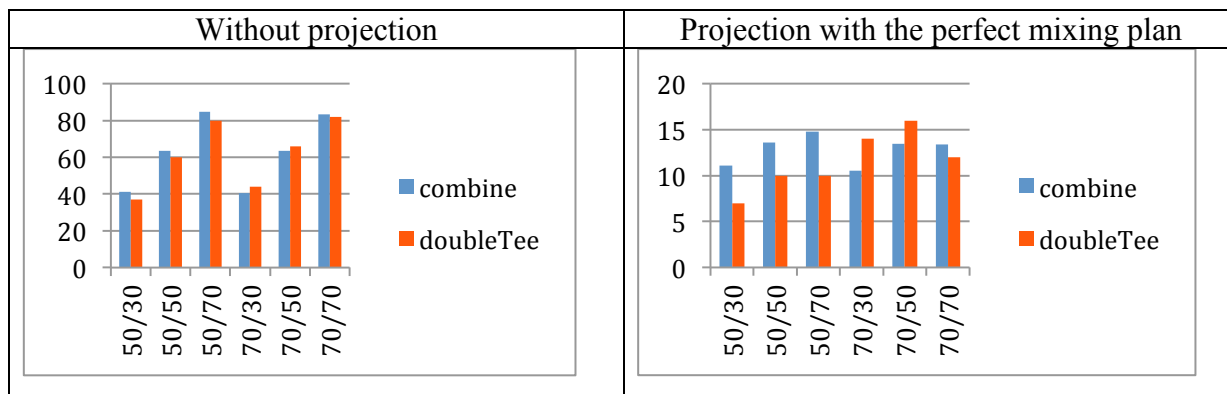


Figure 25: Comparison combined, 5D Re=5,000.

Conclusion:

To accelerate the convergence with CFD simulation that require fewer cells, it was decided to combine two single T simulations to solve the double T problem. It has been found by comparison between full double T simulations and combined single T simulations that this method is working in laminar case for most scenarios. It doesn't work for turbulent cases.

8. Complex Mesh

The real geometry of the experiment case is for example the one described in **Figure 26**. Some large deviations were observed between CFD simulation with and experimentation (*cf.* **Figure 28**). It is important to know if the precise modelling of the double T is necessary. It is possible that eddy turbulence phenomenon at elbows may change the mixing ratios at the end. The complex mesh of **Figure 27** was generated. It is a 2 million cells mesh generated under Salome software [9].

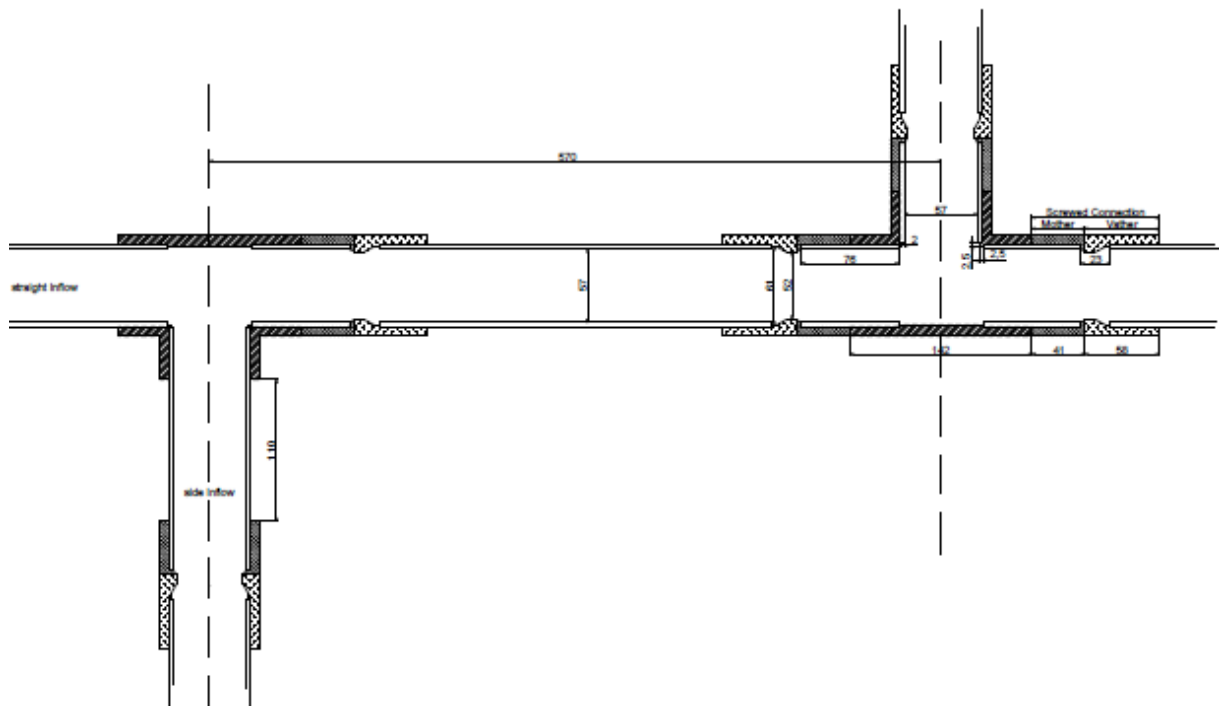


Figure 26: Real geometry.

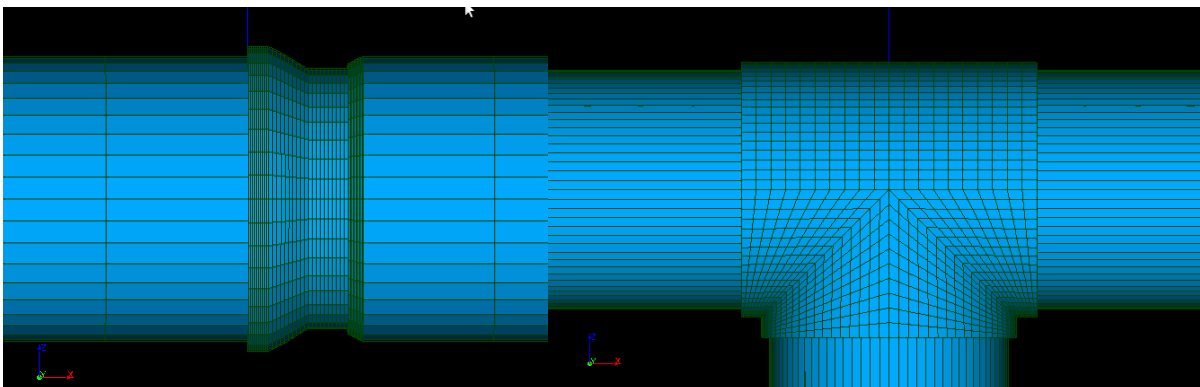


Figure 27: Complex mesh.

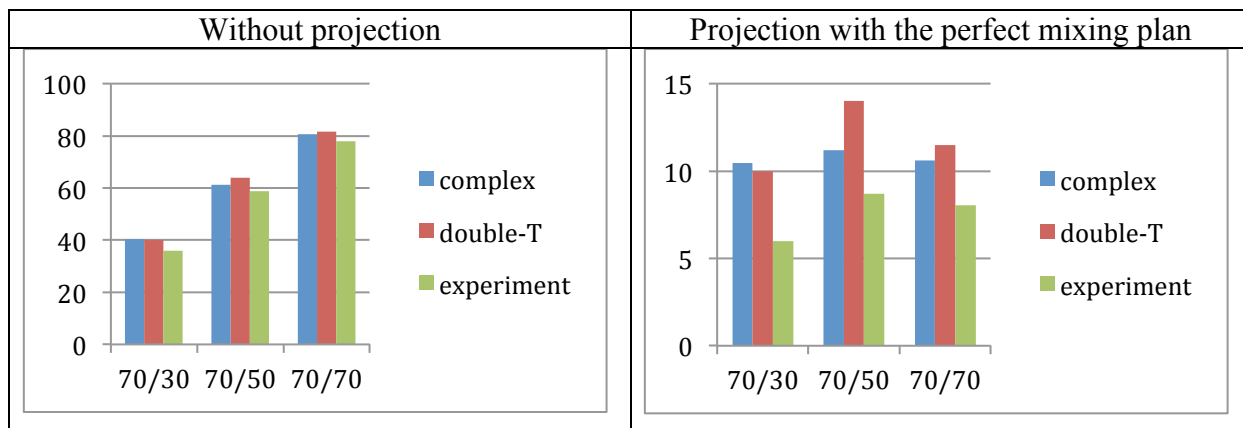


Figure 28: Comparisons of complex geometry, normal geometry and experimentations.

The case 5D, $Re=5,000$, 70/(30 ; 50 ; 70) have been simulated but no large deviations can be observed from the previous simulation of double T with simpler mesh.

Conclusion:

The complex geometry of the double T junction caused by joints doesn't look to affect the results much. It can't explain the differences with the experimentations.

9. Toward a formulation 1D of the imperfect mixing

Let's consider C_1 , C_2 , C_3 and C_4 the mean concentrations on the cross section for the following pipes In1, In2, Out1 and Out2 (cf. **Figure 2**). In the CFD simulation, it has been chosen: $C_1 = 0$ mg/L, $C_2 = 1$ mg/L. We calculate the ratio θ of the average mass flux Q_3C_3 going out of the output 1 divided by the introduced mass flux:

$$\theta = \frac{Q_3C_3}{Q_1C_1 + Q_2C_2}$$

And in the case $C_1=0$ mg/L, $C_2 = 1$ mg/L:

$$\theta = \frac{Q_3C_3}{Q_2C_2} = \frac{Q_3C_3}{Q_2}$$

We then define θ^* as the deviation from the perfect mixing ratio:

$$\theta^* = \theta - \frac{Q_3 * \frac{(Q_1C_1 + Q_2C_2)}{Q_1 + Q_2}}{Q_1C_1 + Q_2C_2} = \theta - \frac{Q_3}{Q_1 + Q_2} = \theta - \frac{Q_3}{Q_3 + Q_4} \quad (20)$$

θ^* is the coefficient saved in the lookup table. θ^* is bounded from below by -1 and from above by +1. In practice θ^* was found in the range [-0.056, 0.361].

From $\theta^*(\%Re_{In1}, \%Re_{In1}, Re, L/D)$, that interpolated at values not in the table by the Kriging method, θ ($\%Re_{In1}, \%Re_{In1}, Re, L/D$) is worked out from **Eq. (20)**.

Therefore, if $C_1 = 0$ mg/L, $C_2 = 1$ mg/L:

$$Q_3C_3 = \theta(\%Re_{In1}, \%Re_{In1}, Re, L/D) * Q_2$$

This can be generalised for any C_1 and C_2 . The mass flux leaving by outlet Out1 is composed of a part coming from In1 and another one from In2, the same for Out2.

$$\begin{cases} Q_3C_3 = \theta_{13} * Q_1C_1 + \theta_{23} * Q_2C_2 \\ Q_4C_4 = \theta_{14} * Q_1C_1 + \theta_{24} * Q_2C_2 \\ \theta_{23} = \theta \end{cases}$$

We have a system of three equations and six unknowns (C_3 , C_4 , θ_{13} , θ_{23} , θ_{14} , θ_{24}), because we know the flows, C_1 and C_2 . To resolve the system, we need three more constraints, they can be found as followed.

- When $C_1 = 0$, the mass-balance between inlets and outlets must satisfied:

$$(Q_1C_1 + Q_2C_2) = Q_2C_2 = (Q_3C_3 + Q_4C_4)$$

So

$$Q_2C_2 = \theta_{23} * Q_2C_2 + \theta_{24} * Q_2C_2$$

Assuming that Q_2C_2 is not zero leads to:

$$\theta_{24} = (1 - \theta_{23})$$

- Similarly, when $C_2 = 0$ and $Q_1 C_1$ is positive, we get:

$$\theta_{14} = (1 - \theta_{13})$$

- Finally, for $C_1 = C_2 > 0$, the mixing of fluids of similar concentration should give a fluid of same concentration, $C_3 = C_4 = C_1 = C_2 > 0$:

$$\begin{cases} Q_3 = \theta_{13} * Q_1 + \theta_{23} * Q_2 \\ Q_4 = \theta_{14} * Q_1 + \theta_{24} * Q_2 \end{cases}$$

$$then \begin{cases} \theta_{13} = \frac{Q_3 - \theta_{23} * Q_2}{Q_1} \\ \theta_{14} = \frac{Q_4 - \theta_{24} * Q_2}{Q_1} \end{cases}$$

This gives four more equations from which three are independent, for example:

$$\left[\theta_{13} = \frac{Q_3 - \theta_{23} * Q_2}{Q_1} ; \theta_{24} = (1 - \theta_{23}) \text{ and } \theta_{14} = (1 - \theta_{13}) \right]$$

$$\Rightarrow \theta_{14} = \frac{Q_4 - \theta_{24} * Q_2}{Q_1}$$

We have six equations for six unknowns that can be reduced to four equations with four unknowns:

$$\begin{cases} Q_3 C_3 = \theta_1 * Q_1 C_1 + \theta_2 * Q_2 C_2 \\ Q_4 C_4 = (1 - \theta_1) * Q_1 C_1 + (1 - \theta_2) * Q_2 C_2 \\ \theta_2 = \theta \\ \theta_1 = \frac{Q_3 - \theta * Q_2}{Q_1} \end{cases} \quad (21)$$

C_3 and C_4 can be calculated from θ , C_1 , C_2 and the flows rates.

Those equations permit to define a law that can be used for every double T-junction (with equal diameters).

Conclusion:

CFD simulation results have helped to fill a lookup table with a non-dimensional indicator of the deviation from the perfect mixing. It is derived a system of equations than generalises the case introduction of a contaminant only at inlet 2 to both of inlets.

10. Implementation

We report here the implementation of the imperfect mixing function to upgrade the transport module of Porteau by Irstea partner. As illustrated in **Figure 29**, one function has been created by Irstea that returns the concentrations at the two outlets of a double T given the four parameters and using system of equation **Eq. (21)**. For the Cross junction case it is to be provided by IOSB. Optionally it will be possible to use the BAM or the AZRED models (even if there are not complete of the full range of Reynolds). The C++ DLL library was shared with the 3S Consult partner.

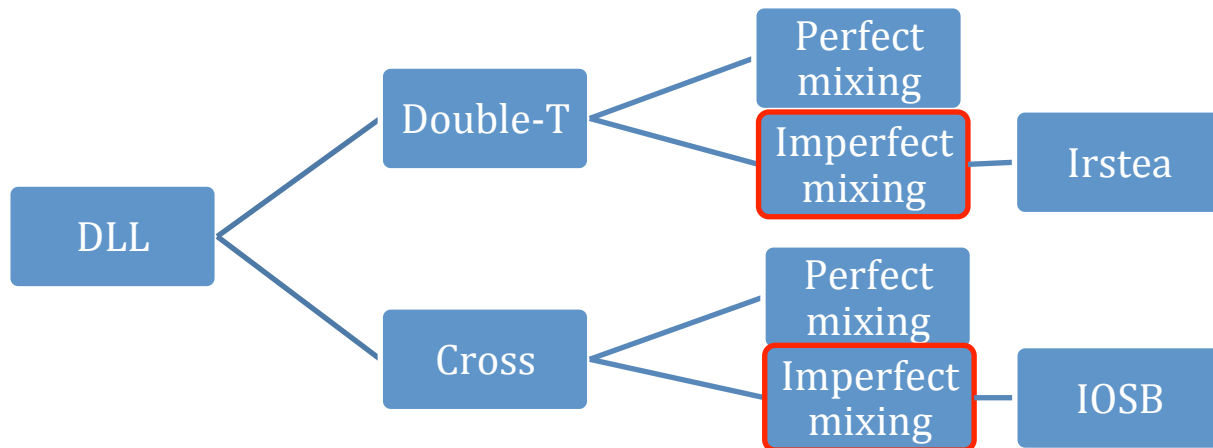


Figure 29: Choices for transport calculation, Cross and Double T.

Conclusion:

The imperfect mixing function has been implemented under the form of a dynamic library in C++ that is connected to the Porteau and the Sir 3S software solutions. This DLL solves the transport-reaction equation through every pipes of a given network and additionally perfect or imperfect mixing is applied at some specific junction nodes, if outlets of N or X-junctions.

11. Conclusion

The imperfect mixing at cross and double T-junctions was studied recently for water distribution networks in the literature. It has led to releasing the models BAM and AZRED. We proposed to complete these studies by carrying out 3D CFD simulations for the full range of Reynolds number (including laminar) and experiments. Two CFD simulation tools have been used mainly, Code Saturne for direct numerical simulations (DNSs) and Fluent for Large Eddy Simulation (LESSs). The simulations have been launched on the Irstea computational grid and on the MCIA. Additional simulations to test convergence of the grid have been made on the CINES.

The computational cost justifies the use of a Delaunay method to optimise the repartition of simulation points. A high order interpolation have been used, the Kriging method. It is coupled with the Delaunay method and is used for the interpolation of the 1D imperfect mixing law. It shows that the Delaunay triangulation is a simple and efficient method to find new point of simulation by reducing the error of interpolation.

The contamination was introduced to one of the two inlets, namely inlet Int2. The results show that perfect mixing still occurs when inlet int2 is dominating. It is due to the fluid coming from the entry 2 going straight to the wall, creating a lot of turbulence. In other cases we observe imperfect mixing with a peak at around $\%In2=30$.

Comparisons with experimentations have shown that there might be a need to take into account the gravity phenomena for low Reynolds numbers. For higher Reynolds, the simulations and experiments agree, and remaining differences between them may be explained by the gravity effect with a sensor at the centre of the pipe.

Some more tests have been made, first the acceleration of the simulations by combining two single T-junctions. It gives good results for laminar cases but does not work for turbulent cases. Also, there is the use of a complex mesh taking into account the real geometry of the double T used in the experiments. No significant improvement has been observed with the complex mesh.

A 1D transport model was created and implemented. It considers advection/reaction along pipes, imperfect mixing for cross and double T, and perfect mixing for simple junction nodes. For imperfect mixing the mean cross-sectional concentration at the two outlets is calculated. The result depends on the Reynolds number at half distance, on the two inlet and outlet flow rate ratios and on the inter-T length. A lookup table was deduced from the CFD simulations, and a Kriging method is used for points that are not on the grid. The transport model takes the form of a DLL in C++ that can be indifferently called from the Irstea (Porteau) or from the 3S consult (Sir 3S) software solutions.

It works for crosses and double T with similar diameters with for the last case an interpipe length of at least five diameters. The user can choose independently the method to use for cross/double T: perfect or imperfect-mixing.

12. Acknowledgements

We want to acknowledge the two following institutes for letting us use their computation cluster to carry out the simulations performed in this project part:

- *Mésocentre de Calcul Intensif Aquitain (MCIA), Avakas supercomputer*
- *Centre Informatique National de l'Enseignement Supérieur (CINES), Jade supercomputer*

Bibliographical references

- [1] Ho, C.K., and S.S. Khalsa, 2008, EPANET-BAM: Water Quality Modeling with Incomplete Mixing in Pipe Junctions, in Proceedings of the 2008 Water Distribution System Analysis Conference, Kruger National Park, South Africa, August 17-20, 2008. (SAND2008-3065C), 11 pages.
- [2] Choi, C. Y., Shen, J. Y., and Austin, R. G. 2008. Development of a Comprehensive Solute Mixing Model (AZRED) for Double-Tee, Cross, and Wye Junctions. Water Distribution Systems Analysis 2008, 1-10.
- [3] EPANET-BAM (2013). <http://www.sandia.gov/epanet-bam/>, accessed on April 23, 2015.
- [4] Porteau 2015, <http://porteur.irstea.fr/>, accessed on April 3, 2015.
- [5] Sir 3S 2015, <http://www.3sconsult.de/sir3s.html> , accessed on April 3, 2015.
- [6] Ung, H., Piller, O., and Gilbert, D. (2014). "Quasi-real time modeling for security of a drinking water distribution network." Procedia Engineering, 70, 800-809.
- [7] Braun, M., Bernard, T., Ung, H., Piller, O., and Gilbert, D. (2014). "Model based investigation of transport phenomena in water distribution networks for contamination scenarios." Procedia Engineering, 70, 191-200. .
- [8] Ansys Fluent 2014,
http://www.ansys.com/fr_fr/Produits/Flagship+Technology/ANSYS+Fluent , accessed on May 6, 2014
- [9] Salome, <http://www.salome-platform.org/>, accessed on April 23, 2015.
- [10] Mésocentre de Calcul Intensif Aquitain (MCIA)
- [11] Code Saturne 2014, <http://code-saturne.org/>, accessed on May 6, 2014.
- [12] CINES, <https://www.cines.fr/>, accessed on April 3, 2015.
- [13] Cressie, N 1993: Statistics for spatial data, Wiley, New York
- [14] Dace, <http://www.imm.dtu.dk/~hbni/dace/> accessed on April 3, 2015
- [15] M. Bergmann, A. Iollo, H. Telib. Project No:ACP8.GA.2009.233665. FFAST Future Fast Aeroelastic Simulation Technologies D2.17: Implementation and validation of hybrid basis fusion ROM method. , Inria 06/13/2012.